OPTICAL SIGNAL PROCESSING FOR EFFICIENT INFORMATION NETWORKS

by

Jasper R. Stroud

A dissertation submitted to The Johns Hopkins University
in conformity with the requirements for the degree of
Doctor of Philosophy

Baltimore, Maryland
July, 2019

Abstract

With the internet and rise of personal electronics there is an ever increasing amount of data collected and transmitted every day; modern communication systems will soon be overwhelmed. The driving force behind the demand is an increasing speed of signal acquisition, in the public domain, as well as medicine and industry; newer technologies allow massive amounts of data produced through text, voice, and video. This puts strain on both signal acquisition systems and communications systems to increase the total information flow. Transmission down fiber links is enabled by the large but limited bandwidth of optical fiber, and as we look toward the future, efficient use of the available optical bandwidth is paramount. I apply the large bandwidth of fiber and ultrafast speed of nonlinear optics to solve these problems, implementing high-speed and efficient signal acquisition and communication systems.

With the increased volume of information being transferred, compression of data has become essential to allow multimedia communication. Data is acquired then compressed and transmitted, requiring massive computing power. Using the information theory technique coined “compressed sensing”, we demonstrate real time compression at signal acquisition, removing a time-consuming and bandwidth inefficient step in a complete communication link. I use dispersion and nonlinear wave mixing in optical fiber, and gigahertz electro-optics to shape light at terahertz speeds, reaching towards the limit of compressed image acquisition.

To complete a high-speed communications link, I investigate the use of Nyquist optical time division multiplexing to maximize spectral efficiency. The square spectral shape of a Nyquist pulse is ideal, but the pulse ripples on forever in the time domain, presenting problems for demultiplexing Nyquist signals at the receiver. I present a solution using coherent detection with a biorthogonal Nyquist pulse to eliminate interference from neighboring channels, and implement a proof of concept system using nonlinear wave mixing. Stable clock transfer is essential for coherent communication, but environmental fluctuations erode clock information, reducing the effective data rate of the communications channel. I present a versatile solution for stable time and frequency transfer using dispersion and nonlinear wave mixing in optical fiber.

Thesis Committee

Primary Readers

Mark A. Foster (Primary Advisor)
Associate Professor
Department of Electrical and Computer Engineering
Johns Hopkins Whiting School of Eningeering

Trac D. Tran
Professor
Department of Electrical and Computer Engineering
Johns Hopkins Whiting School of Eningeering

Alternate Readers

Amy C. Foster
Associate Professor
Department of Electrical and Computer Engineering
Johns Hopkins Whiting School of Eningeering

Acknowledgments

I would like to thank doctors Kieth Petrillo, Nelli Mosavi, Fred Davidson, Jacob Khurgin, Trac Tran, A. Brinton Cooper, Amy Foster, and Mark Foster for phenomenal teaching, advice, and guidance.

I would also like to thank my colleagues Milad Alemohammad, Jeff Shin, Bryan Bosworth, Neil MacFarlane, Kangmei Li, Hongchenge Sun, Hong-fu Ting, Ke-yao Wang, LuoLuo Li, and Dung Tran.

Lastly, thank you to my family for supporting me throughout.

Table of Contents

List of Tables

List of Figures

Chapter 1

Introduction

1.1 Thesis statement

Before the first optical fibers lit up the bottom of the oceans, light based technology had revolutionized how we can interact with each other and the world. In order to enable future innovation such as petabyte communication, exotic wave detection, and high-volume imaging we must continue to push technology to its limit. The massive capabilities of optics can only be harnessed by optical-to-optical interactions. In this thesis I will present multiple techniques that use light to control light, pushing the limits of signal processing.

1.2 Motivation

Today we have a vast data network that spans throughout the globe, and with the recent rise to information sharing we have finally begun to light up the dark optical fibers laid down in the past few decades (Hecht, 2004). There has been a tremendous amount of progress in increasing the speed and capacity of network nodes, but data collection is increasing at a faster rate beginning to overflow modern networks (Kachris, Kanonakis, and Tomkos, 2013). What this means for data networks is each node generates and demands more bandwidth, not only straining the capacity of the network's main pipelines, but demanding efficient and robust signal processing and network control. New solutions are needed to satisfy the requirements of next-generation communications networks. There are two macro-solutions to enable growth, primarily by increasing speed of data flow using newer technology, and secondarily through differentiating between data and information.

Fiber optics has become an essential part of communications and sensing equipment. The development of low loss fiber and erbium doped fiber amplifiers in the 1970s and 80s opened up a huge window for communications in the optical spectrum. The massive amount of capacity suddenly available overwhelmed demand in the 90s, factoring into the following dot com and telecom bubble (Hecht, 2004; Malik, 2003). Further research and development has continued to improve the robustness of optical networks, where today we are starting to see optical fiber connecting to individual residences, marking the final step of an all-optical information distribution network (Shumate and Snelling, 1991). With the infrastructure almost complete, the improvements needed in network nodes and links have moved beyond the solutions presented with modern digital signal processing technology, where the bandwidth is limited by electronics. Only light can match the bandwidth of light, meaning information technology needs to move from electro-optic signal processing toward optical-optical signal processing.

Over the past couple of decades consumer technology, social media, and big data have exploded the amount of data that is collected and transmitted.

Big data, for example, has become extremely popular in both academia and industry, trying to answer the question; what information can we extract from large amounts data (Lohr, 2012)? Additionally, compression of digital media has enabled sending and receiving large files based on the fact that real images and signals have a much lower information content than the data required to store or collect them would suggest (Wallace, 1992). In response to the massive amount of data, research and industry have started to question traditional methods of signal acquisition to maximize information content and minimize cost. Simply, this means information acquisition systems need to smart, able to extract the information in signals from noise or redundancy by knowing how, where, and when to look.

The combination of maximizing network speed and capacity along with isolating information from data demands the flexibility and bandwidth of optical-optical control. Ideally, an optical signal can transmit terahertz of information from node to node without needing to be decomposed or slowed down due to electronic limitations.

The work presented in this thesis will provide a number of potential solutions for high-speed and robust processing of optical signals. From bandwidth efficient communications to high-speed medical imaging, I demonstrate how optical-optical control of light can enable the next generation of communications networks and signal acquisition systems.

1.3 Key concepts

1.3.1 Fiber optics

First demonstrated by trapping light inside streams of water, total internal reflection is the core principle of fiber optics, allowing for the confinement of light inside glass fibers (Hecht, 2004; Kapany, 1960). Today, fiber optics is known best as the backbone of the internet, due to its ability to transmit light long distances with extremely low loss.

Optical waveguides confine light along in the glass fiber, only suffering from material loss of the very transparent silica. Total internal reflection is achieved when two conditions are met. First, light in a high index of refraction material must be incident to a lower index material, where the index of refraction is the ratio between the phase velocity of the light v and the speed of light in a vacuum $n_{material} = \frac{c}{v}$. Additionally, the angle of incidence has to be larger than the critical angle, which is determined by the index difference between the two materials. Total internal reflection can be maintained along an entire length of fiber because the internal core has a higher index of refraction than the surrounding cladding, $n_{core} > n_{clad}$, together making up an optical fiber.

Not only do the material properties affect the propagation of light, waveguide effects that depend on the size of the core and difference in index of refraction between the core and cladding determine the shape, speed, and number of modes that propagate. (Kapany and Burke, 1961; Agrawal, 2000). When the waveguide is small enough compared to the wavelength of light, only a single mode is allowed to propagate so inter-modal effects are removed, this is called a single-mode fiber (SMF). This thesis will focus on use of various single-mode fibers, so only the fiber material and waveguide properties of dispersion and nonlinearity will be discussed.

Standard single mode fibers are made of silica, designed for operation at 1550 *nm* with a core diameter of 8-10.5 *um* and cladding diameter of 125 *um* with a very small index of refraction difference $n_1 \approx n_2$ (*Corning SMF 28 Ultra Optical Fiber* 2014). The index difference is chosen to maximize the size of the core to ease coupling light into the fiber while maintaining single-mode condition, and the cladding diameter is optimized to produce a flexible and sturdy fiber.

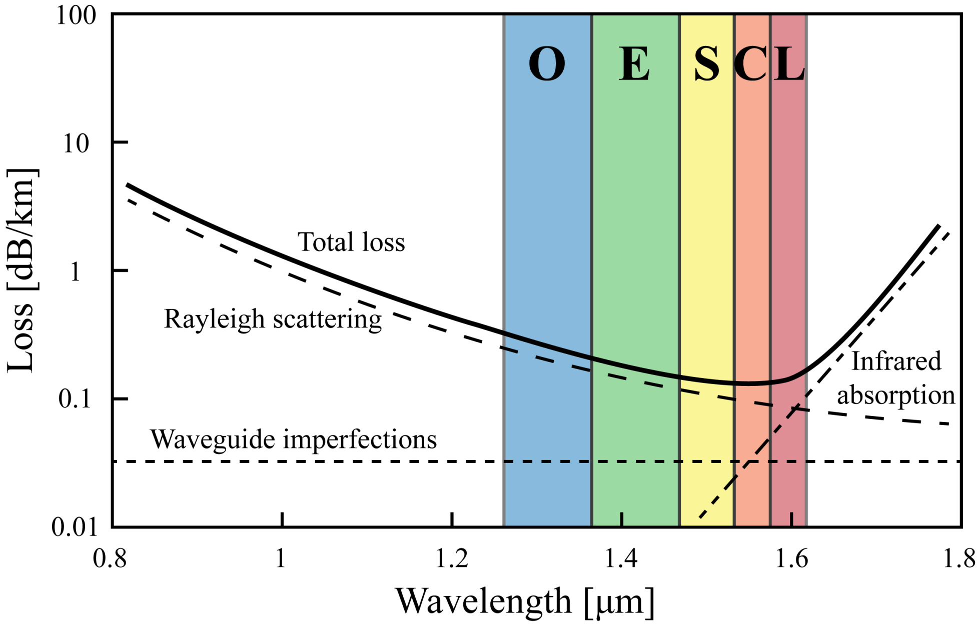

Figure 1.1: The optical loss of a signal down fiber in terms of dB per kilometer in the near-infrared. The communications bands original (O), extended (E), short (S), conventional (C), and long (L) are shown, with the C-band from 1530 *nm* to 1565 *nm* showing the lowest loss <0.2 $[dB/km]$.

Corning SMF-28 has less than 0.2 $[dB/km]$ of loss over a wide range of wavelengths 1490 *nm* to 1625 *nm*, or over 15 *THz* of bandwidth (*Corning SMF*

28 Ultra Optical Fiber 2014). This has enabled the fiber networks we have today, with portions of this spectrum being sectioned for communications, most notably the C-band 1530 nm to 1565 nm, show in Fig 1.1. This massive capability of fiber optics inspired a new industry of optical communications, generating a plethora of passive fiber components such as wavelength division multiplexers, couplers, circulators, optical delay lines, and polarization controllers together enabling a complete and flexible optical network (Lefevre, 1980; Kach, 1979; Tomlinson III, 1978). This thesis will demonstrate a use of passive optical components, standard and specialty fiber, electro-optic devices, and nonlinear wave mixing to construct novel optical signal processing systems that fully utilize the bandwidth of fiber optics.

1.3.2 Chromatic dispersion

The transverse electromagnetic wave propagates through a silica fiber at speeds depending on the size of the core, index of refraction difference between core and cladding, and their material properties. Silica has an index of refraction of $n_{silica} = 1.46$ at $\lambda = 1550\ nm$, but material index of refraction is wavelength dependent, resulting in a wavelength dependent change in propagation time through a fiber.

The waveguide dimensions also provide a wavelength dependent velocity, resulting in the waveguide index of refraction, adding an additional wavelength dependent term to the total effective index of the propagating mode. This effective refractive index $n_{eff}(\lambda) = n_{material}(\lambda) + n_{waveguide}(\lambda)$ determines the speed at which each wavelength travels through the optical fiber (DiDomenico, 1972).

This wavelength dependent change in refractive index results in what is called group velocity dispersion (GVD), the group delay dispersion parameter $D(\lambda) = -\frac{\lambda}{c}\frac{d^2n}{d\lambda^2}$ describes how a wave travels through a uniform material. If $D < 0$ shorter wavelengths will travel faster than longer wavelengths and if $D > 0$ longer wavelengths will travel faster than shorter wavelengths.

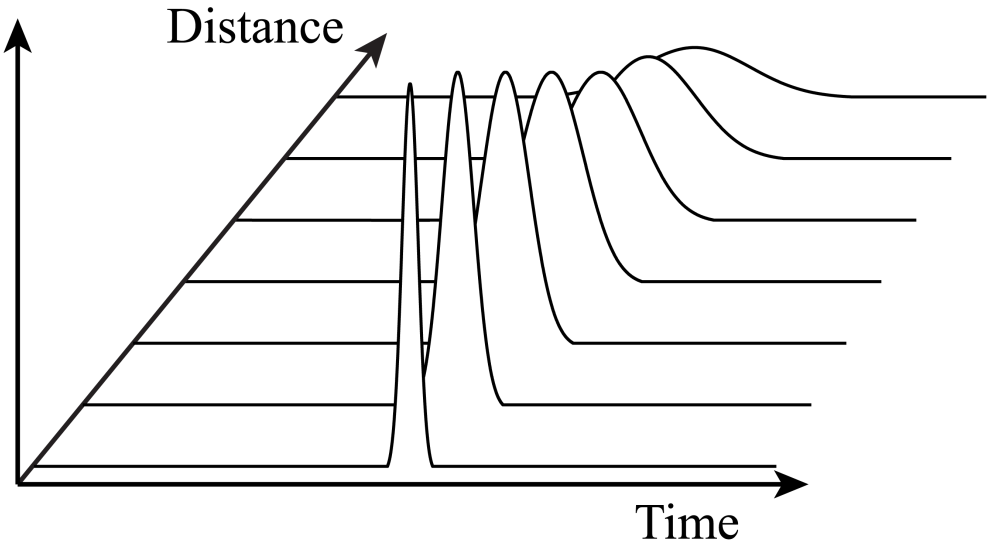

Figure 1.2: An optical pulse travels down a dispersive fiber, |D|>0, spreading out as it propagates, reducing the peak power and increasing the pulse duration.

An optical pulse that has some wavelength dependent time mapping is chirped, and can be compressed back to transform-limited pulse duration. Figure 1.2 shows how propagating down an optical fiber can spread a pulse out, potentially distorting any information due to pulses spreading into one another or fading below the noise floor. When describing the effects of dispersion on an optical pulse, it is convenient to look at how it effects the phase velocity ϕ. This is manifested in a frequency dependent propagation constant

$\beta(\omega)$ that can be expanded in a Taylor series around ω_0 as

$$\beta(\omega) \approx \beta_0 + \beta_1(\omega - \omega_0) + \frac{\beta_2}{2}(\omega - \omega_0)^2 ... \tag{1.1}$$

where β_n is the n_{th}-order propagation constant. The third term β_2 represents the second order dispersion, producing a frequency dependent delay of the spectral components. This spectral phase shift applied by dispersive propagation depends on β_2 as well as the total length L of fiber propagated. The applied electric field $E(\omega)$ will undergo a quadratic spectral phase shift scaled by $\beta_2 L$, and the resulting electric field $E_{disp}(\omega)$ can be described as

$$E_{disp}(\omega) = E(\omega) e^{-j\frac{\beta_2 L}{2}(\omega - \omega_0)^2} \tag{1.2}$$

excluding higher order dispersion terms. Generally third and higher orders of dispersion β_{3+} are negligible, although propagation through long lengths of fiber L>10 km or using large bandwidth optical pulses $BW_{MLL} > 1\ THz$, the effects becomes significant (Agrawal, 2000).

1.3.3 Nonlinearity

In a linear materials we can describe the polarization density field as a scalar function of the applied electric field $P = \epsilon_0 \chi_e E$, where ϵ_0 is the free space permittivity, and χ_e is the electric susceptibility (Feynman, Leighton, and Sands, 1964).

Nonlinear materials respond to the intensity of an applied electric field, resulting in intensity dependent terms in the polarizability of the material.

The polarization density can be described using a Taylor series expansion,

$$P = \epsilon_0(\chi^{(1)}E + \chi^{(2)}E^2 + \chi^{(3)}E^3 + ...) \tag{1.3}$$

where $\chi^{(n)}$ are the $n_{th} - order$ susceptibilities of the material. χ_e is related to the index of refraction by $n = \sqrt{(1+\chi_e)}$ (Agrawal, 2000). The first term in P describes the linear response of the material, $\chi^{(1)}$, and the following are nonlinear terms that alter the index of refraction depending on the material susceptibility and intensity of the applied electric field. Silica is a centrosymmetric material, therefore it has a non-existent second order susceptibility $\chi^{(2)} = 0$, so this thesis will focus on nonlinear interaction based on the $\chi^{(3)}$ term (Levenson and Bloembergen, 1974). With the higher order terms being negligible in most materials, we can define a nonlinear index of refraction related to the effective index as $n(\lambda, I)_{eff} = n(\lambda) + n_2 I$ that is dependent on the intensity of the applied electric field. The nonlinear parameter γ is defined by material and waveguide properties as,

$$\gamma = \frac{2\pi n_2}{\lambda_0 A_{eff}} \tag{1.4}$$

where A_{eff} is the effective area of the mode in the waveguide, and the nonlinear index n_2 is related to material properties (Agrawal, 2000).

When a single wavelength or optical pulse of light travels through nonlinear materials, it can experience self phase modulation (SPM), which can result in spectral broadening, or third harmonic generation (THG), creating light at three times the frequency of the input light $3\omega_0$. Following, when multiple wavelengths of light interact, effects such as cross phase modulation (XPM) and four-wave mixing (FWM) become relevant, specifically FWM generates new wavelengths of light based on the combination of applied fields and will be discussed in more detail.

1.3.4 LASERs and mode-locking

The term LASER is the acronym "Light amplified by stimulated emission of radiation", and has become one of most influential devices in the last few decades. Any LASER consists of a cavity, gain medium, and energy pump shown in Fig 1.3. The gain medium converts the pump energy into light that builds up in the cavity and produces a coherent monochromatic light beam.

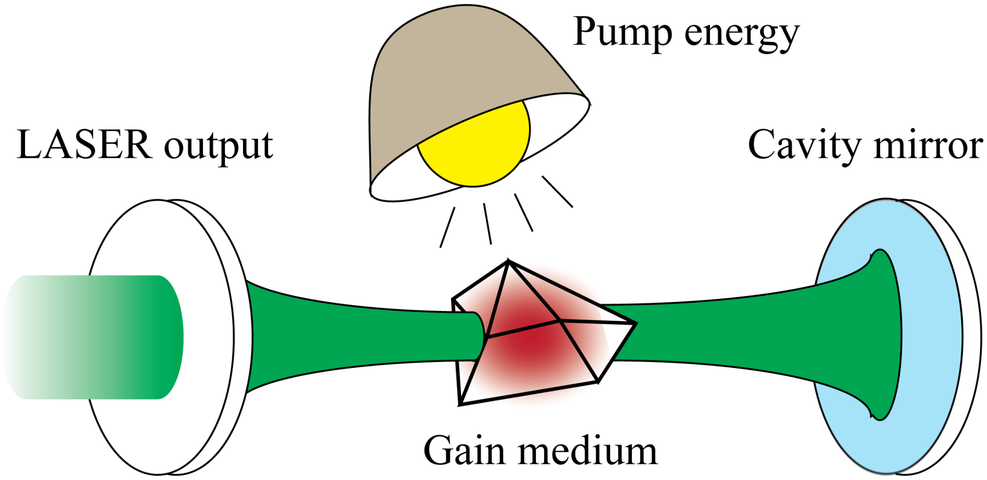

Figure 1.3: A LASER consists of an optical cavity with a gain medium that is externally pumped. The spontaneous emission excites modes of the cavity that can propagate and receive gain through stimulated emission.

The light generated in the gain medium relies on absorption and emission of optical radiation. The energy source, either optical, as shown in Fig. 1.3, or electrical, excites the active atoms in the gain medium, raising their energy level as shown in Fig. 1.4. Spontaneous emission occurs when the excited atoms relax, emitting a photon with energy corresponding to the energy difference between the higher and lower state $\Delta E = E_1 - E_0$. This process is shown in Fig. 1.4 where a pump photon of energy E_2 is absorbed, and after some time $\tau_{21} + \tau_{10}$, a photon is spontaneously created from the relaxation. Similarly, stimulated emission occurs when a photon passes through an atom with a raised energy, stimulating the generation of a additional photon that is the same wavelength and phase of the passing photon. This process, is shown in Fig. 1.4, where both a pump photon and lasing photon pass into the atom, and two coherent laser photons are generated. The initial spontaneous emission that is parallel with the cavity, shown in Fig. 1.3, builds and passes through the gain medium multiple times. This effect eventually starts the cascading stimulated emission of light waves inside the cavity producing monochromatic and coherent light beams known as LASERs (Gould et al., 1959).

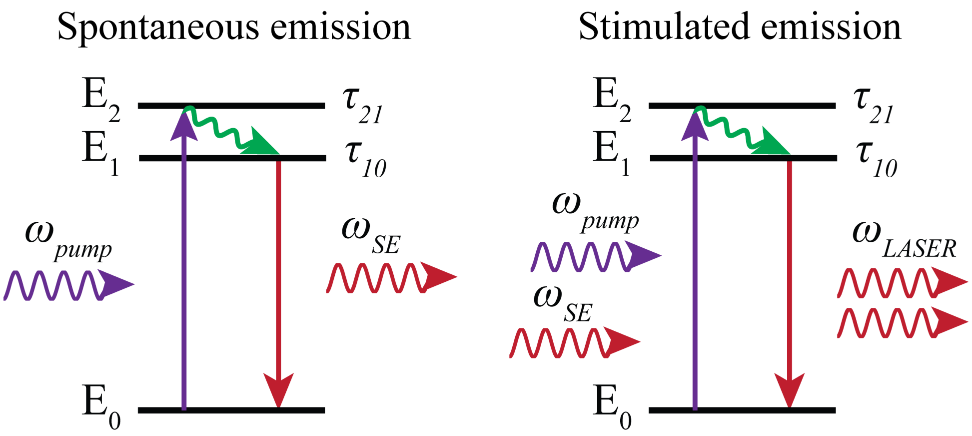

Figure 1.4: The energy diagrams of the spontaneous and stimulated emission process. The spontaneous emission occurs after some relaxation time τ_{21}, but if another photon interacts with the atom, stimulated emission can occur, generating a coherent pair of photons.

Ultrafast optics deals with light interactions at the smallest time scales, using ultrashort pulses with a duration of picoseconds or less. Since the advent of LASERs, research has strived to generate shorter and more stable optical pulses. Mode-locked lasers (MLL) have become the state of the art for creating stable ultrashort pulses. These MLLs can produce extremely short pulses down to a few femtoseconds allowing for high speed communication, medical imaging, interrogation of ultrashort light interactions, and countless more applications (Steinmeyer, 2002; Weiner, 2011).

As suggested by the name, mode-locked lasers generates pulses by locking multiple optical modes that coherently mix to produce a short pulse of light. Simply, this is done by inserting a loss mechanism into the laser cavity that will cause all of the longitudinal cavity modes that are in phase with the loss mechanism to build up and produce an ultrashort optical pulse. The duration of the pulse depends on the bandwidth of the gain material, each longitudinal mode corresponds with a different frequency or wavelength that can propagate in the cavity, the larger the optical bandwidth of the pulse, the shorter it can be in time. Femtosecond MLLs have hundreds of nanometers of optical bandwidth. The rate at which a passively mode locked laser is determined by the cavity dynamics, including the cavity length, the loss mechanism, and other inter-cavity effects (Jones et al., 2000). Figure 1.5 shows how the cavity modes and laser gain bandwidth combine to define a passively MLL spectral profile.

For a Gaussian beam the pulse width is transform limited to $\Delta t_{FWHM} = \frac{0.441}{BW_{FWHM}}$, determined by the full-width half maximum (FWHM) of the laser gain bandwidth. This Gaussian spectral shape corresponds to a Gaussian

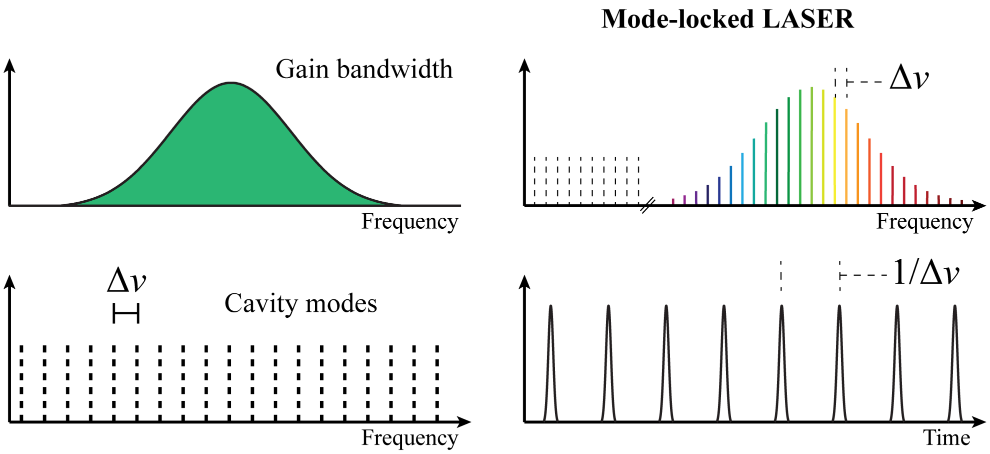

Figure 1.5: The gain bandwidth of the cavity and the modes allowed in the cavity determine the repetition rate and bandwidth of the MLL. The laser output pulses at the inverse of the mode separation $\Delta\nu$.

temporal profile, shown in Fig. 1.5. Non-Gaussian gain spectra, internal cavity filters, or external manipulation of the spectrum can produce different temporal profiles. Generally, this is know as pulse shaping, a huge arm of research with a variety of applications in communications and signal processing (Weiner, 2011).

1.3.5 Optical amplification

Signals propagating down some medium incur loss, although optical fiber has extremely low loss a signal sent from one side of the Atlantic could not make it across to the other side. Maintaining the optical signal to noise ratio is paramount for long-haul data transmission. Networks can employ optical repeaters that detect a transmitted signal after some distance of fiber, then re-transmit the signal further down the line. This optical-electrical-optical conversion is power consuming and increases the system complexity, instability, and cost (Becker, Olsson, and Simpson, 1999).

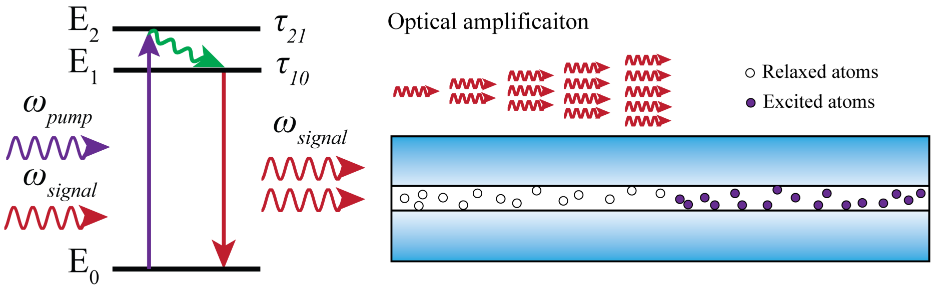

Figure 1.6: The energy diagrams of a three level stimulated emission process that leads to optical gain. Signal light is amplified as it propagates down the excited erbium fiber.

Using the same process that is the core to LASERs, optical amplification can be used to amplify a signal as it propagates down a fiber. For amplification of communications signals, erbium doped fiber amplifiers (EDFA) have dramatically increased the size and information capacity of fiber links. The erbium doped fiber core is generally optically pumped with 1490 nm light that excites the erbium atoms to a higher energy level. As shown in Fig. 1.6, as the C-band light travels through the fiber, stimulated emission amplifies the signal. Erbium allows for a gain bandwidth that stretches over the entire C-band enabling high-throughput long-distance communication.

1.3.6 Specialty optical fiber

Optical fiber for long distance communication is designed for the lowest possible loss, with the state of the art being Corning SMF-28, with less than 0.2dB/km from 1490 nm to 1625 nm. However, the dispersion of SMF in the C-band is $D_{SMF} \approx 18[ps/nm/km]$, meaning longer wavelengths will travel faster than shorter wavelengths (*Corning SMF 28 Ultra Optical Fiber* 2014). As mention earlier, the resulting pulse spreading can limit bit rates. By altering the waveguide dimensions from the standard core diameter of 8-10 um, the waveguide refractive index $n_{waveguide}(\lambda)$ can be altered to change the effective index n_{eff} and consequently the fiber dispersion D_{fiber}. This allows short pulses of light to be stretched out in a positive dispersion waveguide, SMF, then compressed in a negative dispersion waveguide, or dispersion compensating fiber (DCF).

Generally DCF has a decreased fiber core, increasing the waveguide dispersion to mitigate or reverse the effects of material dispersion. Figure 1.7 shows the dispersion over the wavelengths around the C-band, where SMF has positive dispersion and the dispersion-shifted fibers (DSF) have negative or near zero dispersion due to their waveguide dispersion (Gruner-Nielsen et al., 2005).

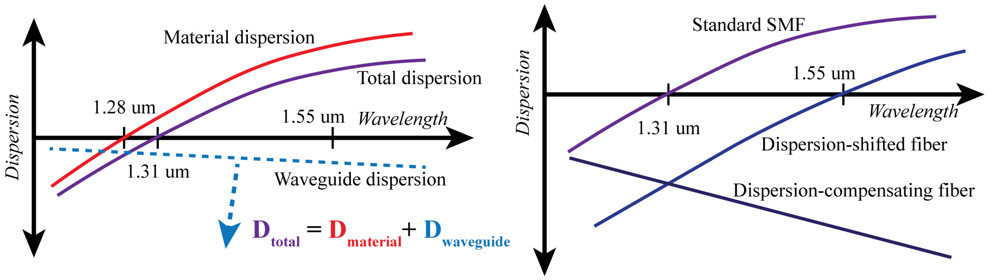

Figure 1.7: The total dispersion in purple is the combination of material dispersion in red, and waveguide dispersion in blue. By altering the waveguide properties, the waveguide dispersion can be increased, resulting in dispersion-shifted fiber (DSF) and dispersion-compensating fiber (DCF).

All materials have a nonzero nonlinear parameter γ causing problems for optical communications through spectral broadening or inter-modulation effects that can distort the information in optical fiber links (Mitra and Stark, 2001). Recent communications research has incorporated nonlinearity directly

Fiber	Loss	Dispersion (D)	Dispersion slope (D_{slope})	Nonlinearity (γ)
SMF	< 0.19 $[dB/km]$	18 $[ps/nm/km]$	0.092 $[ps/nm^2/km]$	1 $[W/km]$
DCF	< 0.27 $[dB/km]$	-38 $[ps/nm/km]$	-0.11 $[ps/nm^2/km]$	4 $[W/km]$
DSF	< 0.21 $[dB/km]$	-4 $[ps/nmkm]$	0.12 $[ps/nm^2/km]$	2 $[W/km]$
HNLF	< 0.9 $[dB/km]$	-0.5 $[ps/nm/km]$	0.019 $[ps/nm^2/km]$	11.5 $[W/km]$

Table 1.1: The optical properties of different fibers at 1550 nm wavelength. The fiber loss is lowest for SMF, but the dispersion requires long distance systems to use DCF and DSF to compensate for the dispersion and dispersion slope. The large nonlinearity of HNLF is paired with a small amount of dispersion to increase phase matching, but suffers from higher loss.

into the modulation and demodulation process to overcome this limit (Gui et al., 2017). However, nonlinearity can offer advantages using effects such as FWM, so some specialty fiber is made to increase the nonlinear parameter γ using its dependence on n_2 and A_{eff} shown in Eq 1.4 for various fibers. This highly nonlinear fiber (HNLF) can be fabricated by doping or creating a micro-structure core to increase the nonlinear index n_2, or reducing the fiber core size and increasing the core-cladding index mismatch to decrease the effective area of the mode A_{eff}. Due to the phase matching conditions required for nonlinear effects, it is important to note the dispersion of the nonlinear fiber, with applications requiring different dispersion profiles to optimize certain nonlinear interactions.

Table 1 shows the parameters of optical fibers at 1550 nm used in this thesis. The dispersion caused by SMF can be compensated for with DCF, and the dispersion slope can be compensated with the proper addition of DSF (*Corning SMF 28 Ultra Optical Fiber* 2014; *Dispersion Compensating Fiber* 2017; *Non-Zero Dispersion-Shifted Fiber* 2018; *Standard Highly Non-Linear Fiber Modules* 2019). Controlled nonlinear reactions using HNLF with appropriate input dispersion are essential to the work presented in this thesis.

1.3.7 Electro-optic devices

The combination of electronics and optics has been essential for both the telecommunications boom as well as providing the camera devices we all use every day. As opposed to the detection of light, electro-optics refers to altering the light inside a material using electronics. This generally done through the Pockels effect, found in materials that lack inversion symmetry, where the effective index of can be modulated by an applied electric field (Chmielak et al., 2011). If we consider applying a voltage $V(t) = \alpha sin(\Omega t)$ with some amplitude α and frequency Ω to the electro-optic device, the phase shift introduced on a wave oscillating at the carrier frequency ω and slowly varying envelope A is,

$$E_{PM} = Ae^{j\omega t}e^{j\alpha sin(\Omega t)}. \tag{1.5}$$

Because α is small, we can use a Taylor series expansion to generate side band around the carrier frequency

$$A(e^{j\omega t} + e^{j\alpha t(\omega+\Omega)} + e^{j\alpha t(\omega-\Omega)}). \tag{1.6}$$

This only includes the first order side-bands, in reality there are infinite at $\pm n\Omega$ where $n = 1, 2, 3....$ This phase modulated signal can be combined with the original field $Ae^{j\omega t}$ to produce amplitude modulation through constructive and deconstructive interference between the phase modulated and non-phase modulated waves. Both phase and amplitude modulation can be used to encode information of a light wave, where the amplitude $\alpha(t)$ or frequency $\Omega(t)$ of the modulation can carry information (Winzer and Essiambre, 2008).

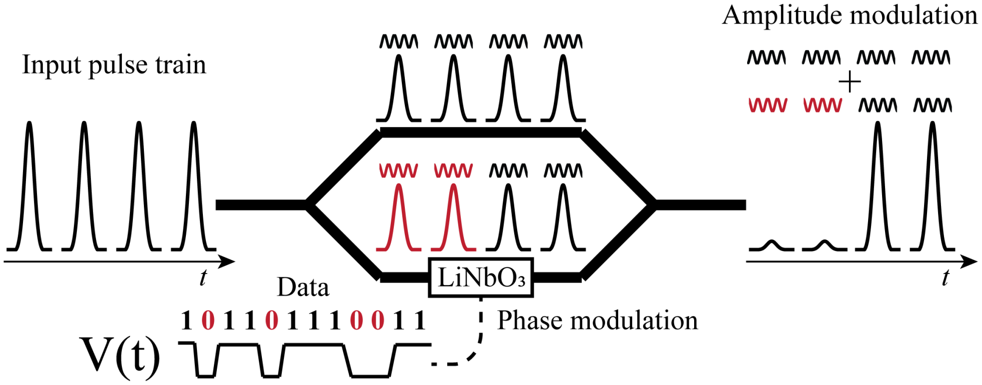

Figure 1.8: Data can be modulated onto the amplitude of a laser pulse using constructive and deconstructive interference. The phase modulator is place in one arm of a mach-zehnder interferometer, where the $LiNbO_3$ phase modulation causes deconstructive interference with the non-modulated arm at the output.

In the C-band, phase modulation can be achieved using a lithium niobate (LiNbO3) waveguide, where the electro-optic $LiNbO_3$ provides a phase change with respect to the applied voltage (Weis and Gaylord, 1985). In an electro-optic amplitude modulator, shown in Fig. 1.8, the input is split using a Mach-Zhender interferometer (MZI), with one arm containing a phase modulator. By applying a voltage V_π, the phase of pulse is shifted by 180°, such that when it is recombined with the other arm of the MZI there is deconstructive interference, converting the encoded information from phase to amplitude.

In addition to electro-optic modulators (EOM), another key electro-optic technology to this thesis is a programmable spectral filter. As mentioned earlier, pulse shaping is essential to optical signal processing, with different pulse shapes having various advantages. One way to control a pulse is using the amplitude and phase of the spectrum, which gives near-complete control over the pulse temporal shape and duration.

Independent wavelength control can be achieved using wavelength to space mapping of a diffraction grating, then applying amplitude and phase shifts to the isolated wavelengths. Similar to an EOM, the light beams travel through electro-optic cells in order to achieve amplitude and phase shifts. The setup for a free space spectral shaper is shown in Fig 1.9, where the input light is spatially mapped onto an array of electro-optic cells. Each cell can be programmed to provide binary, as shown in Fig 1.9, or arbitrary modulation. The output spectrum is recombined using the inverse mapping process, and coupled back into a fiber (Stobrawa et al., 2001).

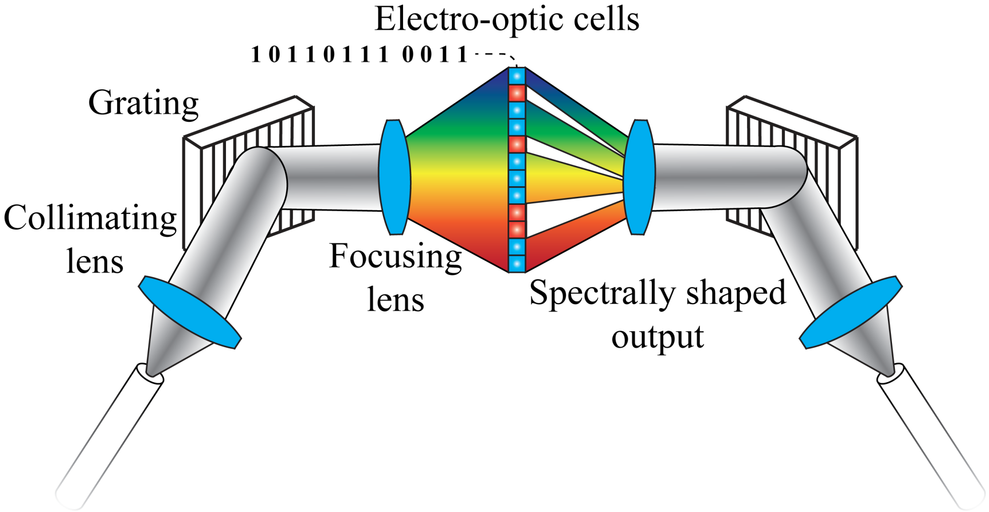

Figure 1.9: The spectrum of an pulse can be spread out using a diffraction grating, then sent through an array of electro-optics cells that can individually control each wavelength.

Although this method of spectral shaping has high precision and dynamic range, the speed at which it can update the programmed patterns is limited by the electro-optic modulation (Stroud and Foster, 2019). This thesis will use this type of spectral shaping and present more exotic techniques for higher speed and more flexible spectral shaping.

1.3.8 Four-wave mixing

Parametric processes refer to lossless nonlinear interactions that occur essentially instantaneously, a quantum mechanical process where photons raise an atoms energy into a virtual state and relaxes near-instantly to produce photons of equivalent energy. This light speed multi-wave interaction can be used for control of light signals at the shortest of time scales.

Of the many nonlinear wave inter-modulation effects from the $\chi^{(3)}$ susceptibility, FWM is the only wave generation technique that can be done with the confinements of the C-band, meaning there is an abundance of telecommunications equipment that can be used to control light around the $1550nm$ wavelength. However, the bandwidth of this nonlinear interaction is not limited to the C-band, potentially spanning over hundreds of nanometers (Wang and Foster, 2012). The term four-wave mixing comes from the terms generated by the $\chi^{(3)}$ when three distinct frequencies are applied to a nonlinear medium and a new frequency is generated, thus a four-wave interaction. The real part of the nonlinear polarization density in a $\chi^{(3)}$ material can be described as,

$$P_{NL} = \epsilon_0 \chi^{(3)} (E_1 cos(\omega_1 t) + E_2 cos(\omega_2 t) + E_3 cos(\omega_3 t))^3 \tag{1.7}$$

which produces the terms using Euler's formula,

$$\begin{aligned}P_{NL} = \frac{\epsilon_0 \chi^{(3)}}{2}(&E_1^3 e^{\pm j3\omega_1 t} + E_2^3 e^{\pm j3\omega_2 t} + E_3^3 e^{\pm j3\omega_3 t} + \\ &3E_1 E_2^2 e^{\pm j\omega_1 t} e^{\pm j2\omega_2 t} + 3E_1^2 E_2 e^{\pm j2\omega_1 t} e^{\pm j\omega_2 t} + \\ &3E_1 E_3^2 e^{\pm j\omega_1 t} e^{\pm j2\omega_3 t} + 3E_1^2 E_3 e^{\pm j2\omega_1 t} e^{\pm j\omega_3 t} + \\ &3E_2 E_3^2 e^{\pm j\omega_2 t} e^{\pm j2\omega_3 t} + 3E_2^2 E_3 e^{\pm j2\omega_2 t} e^{\pm j\omega_3 t} + \\ &6E_1 E_2 E_3 e^{\pm j\omega_1 t} e^{\pm j\omega_2 t} e^{\pm j\omega_3 t}).\end{aligned} \tag{1.8}$$

The first three terms in Eq 1.8, describe self phase modulation, while the rest can be described as four-wave interactions. Including the corresponding propagation constants, the general form of this can be simplified to

$$\begin{aligned}E_{FWM} \approx E_1 E_2 E_3 e^{j(\pm\omega_1 \pm\omega_2 \pm\omega_3)t} \\ e^{j(\pm\omega_1\beta_1 \pm\omega_2\beta_2 \pm\omega_3\beta_3)}.\end{aligned} \tag{1.9}$$

where β_n are the the propagation constants of the different frequency waves ω_n. Excluded from Eq 1.8 and 1.9 is the phase conjugation of the field E_n depending on the sign chosen. The phase conjugated wave is called the signal, and the other two are pumps ω_{pump_1} and ω_{pump_2}. When $\omega_{pump_1} = \omega_{pump_2}$, the so called pump photons come from the same optical source, the process is degenerate, and when $\omega_{pump_1} \neq \omega_{pump_2}$ it is non-degenerate FWM. The converted wavelengths $\omega_{idler} = \pm\omega_{signal} \pm \omega_{pump_1} \pm \omega_{pump_2}$ are idlers waves and notably, they are directly related to the pump waves and phase signal waves. Figure 1.10 shows the energy diagrams for degenerate FWM, where two pump photons are converted into signal and idler photon, where the idler wave is related to the pump waves and phase conjugated signal wave.

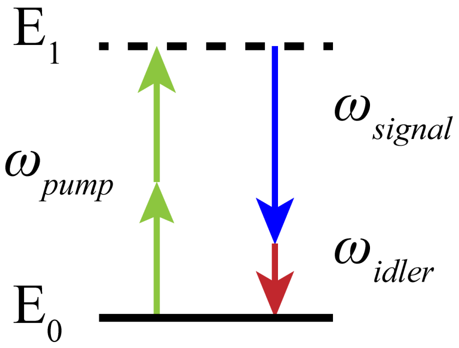

Figure 1.10: The energy diagram shows how the two pump photons in green raise the energy to a virtual state, and two photons the signal in blue, and idler in red are created.

In order for the FWM process to be efficient, the pump and signal waves must be temporally and spatially coherent. While propagation in single mode fiber maintains spatial coherence, the temporal coherence is determined by the difference in propagation constants β_n. This is called phase matching, and is the main limiting factor for the bandwidth of FWM frequency conversion, related to the dispersion in optical fiber (Agrawal, 2000). The phase matching condition for the energy diagrams in Fig 1.10 is defined as,

$$\Delta\beta = \beta_{pump_1} + \beta_{pump_2} - \beta_{signal} - \beta_{idler} = 0. \tag{1.10}$$

Failure to satisfy this phase matching condition will eliminate most of the terms produced simplifying Eq 1.9. Without phase matching techniques, optical power will only flow into the idlers where frequencies $\omega_{idler} \approx \omega_{pump} \approx \omega_{signal}$ such that dispersive effects are minimal. In this thesis, we use standard communications equipment with C-band signal and pump waves to generate idlers also in the C-band. This allows for traditional optical control using passive and electro-optic devices in addition to ultrafast processing using FWM.

1.3.9 Optical time lens

The dispersive effect on a pulse through optical fiber can be described by a change in the envelope $A(z,t)$ of the optical pulse as it propagates down the length $L(z)$ of fiber. The development of the optical envelope can be described as the derivative with respect to z,

$$\frac{\partial A(z,t)}{\partial z} = \frac{j\beta_2}{2}\left[\frac{\partial^2 A(z,t)}{\partial t^2}\right]. \tag{1.11}$$

This is analogous to the diffraction of a spatial beam,

$$\frac{\partial A(z,x)}{\partial z} = \frac{j}{2k}\left[\frac{\partial^2 A(z,x)}{\partial x^2}\right] \tag{1.12}$$

where the envelope $A(z,x)$ describes the spatial beam with respect to x. Matching variables k and β_2 are the propagation constants of the spatial and temporal beams respectively (Salem, Foster, and Gaeta, 2013).

The analogy between temporal and free space optical propagation suggest that more techniques used in spatial optics can be translated to the temporal domain. For instance, a prism can shift the direction of a monochromatic beam by applying a linear phase shift across the beam. Further, lenses focus or diverge light beams by applying a quadratic spatial phase shift through the refraction of light across the curved surfaces. To replicated these effects in the time domain, temporal phase shifts must be applied to optical pulses.

Electro-optic modulators can be used to apply a temporal phase shift. A sine wave voltage signal applied to an EOM can approximate both linear and quadratic phase shifts. The peaks and troughs are approximate to a quadratic, while the zero-crossing is approximately linear. However, in addition approximation errors, the total phase shift and modulation bandwidth is limited by the electronics involved (Kolner and Nazarathy, 1989).

On the other hand, we can use FWM to convert pump photons into signal and idler photons, with a frequency shift on the idler. Using a single wavelength pump, the idler will be an identical copy of the signal, but at the idler frequency $\omega_{idler} = 2\omega_{CWpump} - \omega_{signal}$. Noting that frequency is related to phase through the derivative $\nu = \frac{d\phi}{dt}$, a frequency shift is equivalent to a linear phase shift. Therefore, applying a quadratic phase shift is equivalent to applying a linear frequency shift. This can be done using FWM with a chirped pump pulse instead of the single frequency pump ω_{CWpump}, with dispersion acting as a linear phase shift that the will be applied to the idler. Figure 1.11 shows how the energy diagram for the FWM interaction is time dependent, where the frequency of the chirped pump is time dependent $\omega_{Chirpedpump}(t)$. This applies the linear frequency shift of the dispersed pump onto the idler, a linear frequency shifted version of the signal pulse.

The amount of phase shift applied depends on dispersion β_2 and the length L of fiber used, making it extremely scalable to large phase shifts. Assuming the phase matching conditions are met $\Delta\beta \approx 0$, the idler output from the FWM is related to the signal wave with a phase shit due to pump dispersion. Due to the factor of propagation length L, the FWM time-lens can easily be scaled to large phase shifts.

Similarly to a spatial lens, a time lens can be used to magnify, reduce, or

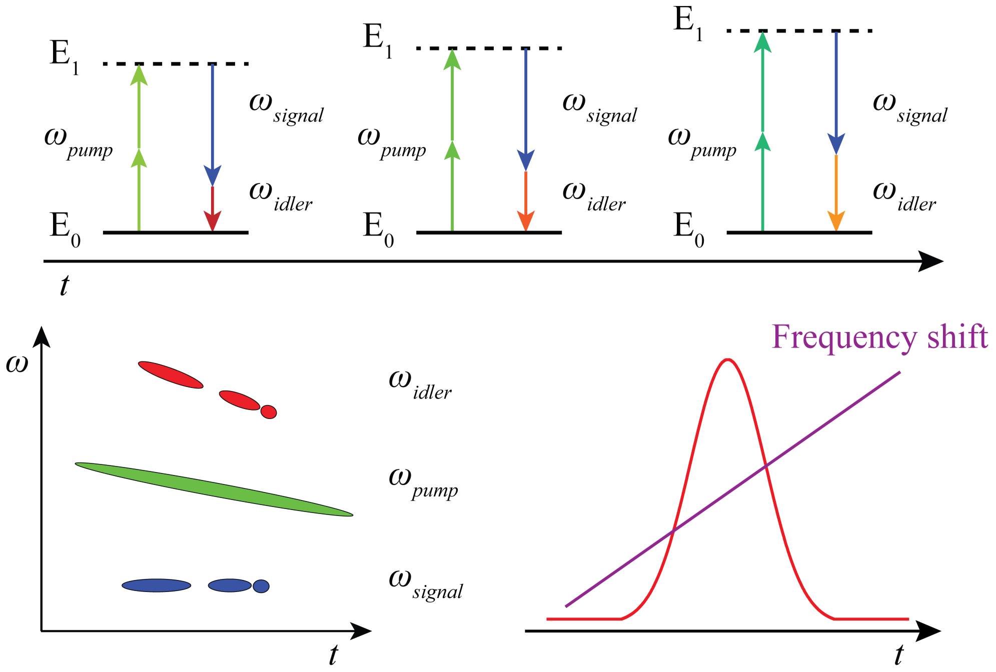

Figure 1.11: Spectrogram of the FWM process and energy diagrams of three different times, showing how the linear frequency shift on the pump to be applied to the idler pulse, shown in red.

Fourier transform a temporal signal. This can be used for a variety of signal processing applications, allowing for high speed control of optical pulses (Salem, Foster, and Gaeta, 2013; Stroud and Foster, 2019; Petrillo and Foster, 2011; Stroud et al., 2018).

1.3.10 Compressed sensing

Compression has become a household term, with modern communication requiring compression to move large amounts of data every day. Common types of compression such as JPEG or JPEG-2000, uses local sparsity of the image after some transform, commonly the discrete cosine transform (DCT) or multi-level wavelet transforms (Wallace, 1992; Marcellin et al., 2000). All compression techniques rely on the assumption that natural images are sparse, meaning in some mathematical basis the signal can be represented by a very small number of significant coefficients.

Traditional sampling is done by taking measurement of the signal amplitude at a constant rate, know as the sampling rate R_b. According to Nyquist theory, to collect the information in a signal the sampling rate must be at least twice the maximum bandwidth of the signal of interest $R_b \geq R_{Nyquist} = 2BW_{signal}$ (Landau, 1967).

However, the total information content of the signal could be much smaller, which is the driving force behind compression theory. This means that the information bandwidth of the signal is far below the sampling rate required by the Nyquist criterion. Figure 1.12 illustrates how mathematical compression is efficient by comparing the under sampling of an image to compression, showing a clearly better image reconstructed using an image transformation.

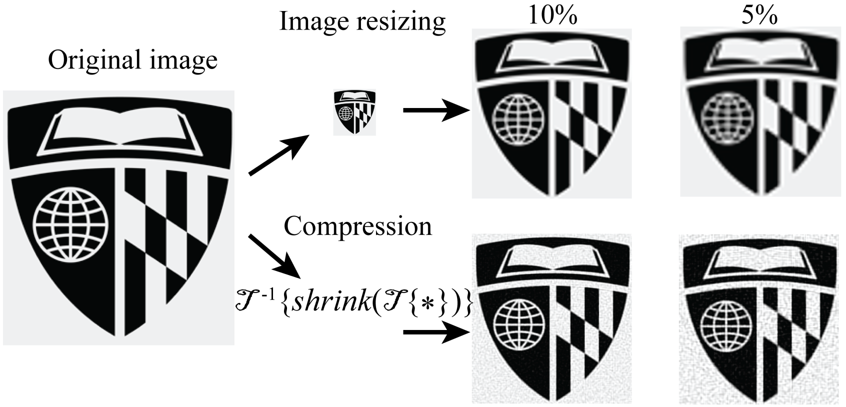

Figure 1.12: A simple compression technique using a transform and inverse transform generates better images than simply reducing the number of pixels. With only 10% and 5% of the original components used, the transform compression maintains higher image quality.

Recent information theory has shown that a sparse or compressible image can be acquired with far fewer samples than required by Nyquist using global image acquisition (Donoho et al., 2006; Eldar and Kutyniok, 2012). By acquiring global information from the signal, each sample contains far more information than the corresponding pixel by pixel sampling required by Nyquist. Without prior knowledge of the sparse domain of a signal under test, global information can be collected by taking a random selection of the signal and integrating it into one sampled value coined "single-pixel" imaging (Stroud and Foster, 2019; Duarte et al., 2008). This is mathematically described as mixing a unknown signal of interest with a known binary pattern, where the compressed measurements can be described as the inner product,

$$y_{CS_i} = \boldsymbol{A}_i x_i \tag{1.13}$$

where A is a known psuedorandom pattern and x is the signal of interest. The signal can be represented in a sparse domain using some sparisfying transform Φ,

$$s = \Phi x \tag{1.14}$$

where s has few non-zero components. The number of compressed samples y_{CS_i} required to reconstruct the signal $i = 1, 2, 3...M$ is related to the sparsity of the signal $klog(N)$, where k is the sparsity, and N is the dimension of the signal, or the number of samples required by Nyquist. Therefore, we can reconstruct signal with far fewer samples than required by Nyquist $M << N$ (Candès and Wakin, 2008).

Using a minimization algorithm, the signal $\hat{x}$ can be reconstructed by minimizing the number of non-zeros components in $\hat{s}$, while maintaining the fidelity of compressed measurement y_{CS} (Figueiredo, Nowak, and Wright, 2007).

$$\min ||\hat{s} - \lambda||_1 \quad \ldots \quad while\ \boldsymbol{A}\hat{x} - y_{CS} = 0. \tag{1.15}$$

Figure 1.13 illustrates the process of a compressed sensing reconstruction algorithm. The compressed measurements y_{CS} and known pseudorandom matrix A used to formulated an initial estimate of the signal $\hat{x}$. This estimate is transformed into the spare representation $\hat{s}$ where the sparsity is enforced by the regularization parameter λ. This sparsified estimate is transformed back in to sampled basis, and the difference between the estimated $A\hat{x}$ and true y_{CS} compressed measurements is minimized. This processes is iterated until the image has been reconstructed, reaching the sparsest solution that maintains the fidelity of the collected measurements.

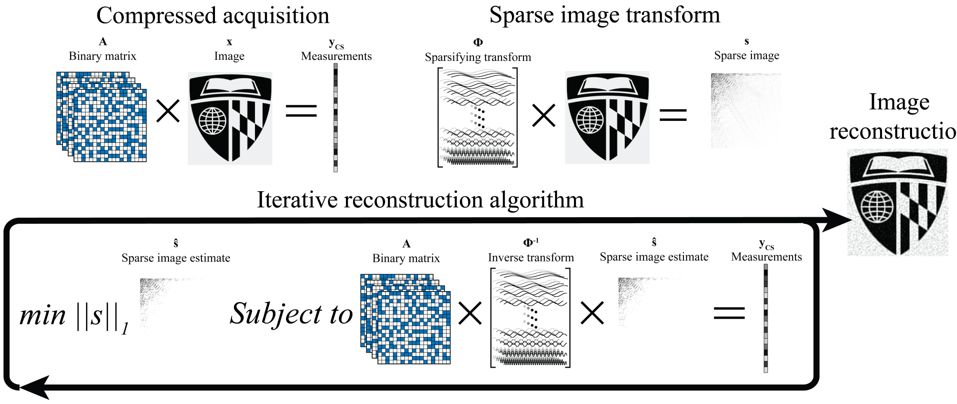

Figure 1.13: The process of a compressed sensing reconstruction algorithm. The compressed measurements y_{CS} and know patterns A are used to generate and image estimate $\hat{x}$. The iterative process finds the sparsest solution using an image transform Φ.

Compressed sensing has revolutionized how signals can be acquired, showing that compression can be achieved simultaneously with acquisition. This thesis will use compressed sensing applied to multiple applications, and will present two methods of collecting compressed data directly using photonic hardware.

References

Hecht, Jeff (2004). *City of light: the story of fiber optics*. Oxford University Press on Demand.

Kachris, Christoforos, Konstantinos Kanonakis, and Ioannis Tomkos (2013). “Optical interconnection networks in data centers: Recent trends and future challenges”. In: *IEEE Communications Magazine* 51.9, pp. 39–45.

Malik, Om (2003). *Broadbandits: Inside the $750 billion telecom heist*. John Wiley & Sons.

Shumate, Paul W and Richard K Snelling (1991). “Evolution of fiber in the residential loop plant”. In: *IEEE Communications Magazine* 29.3, pp. 68–74.

Lohr, Steve (2012). “The age of big data”. In: *New York Times* 11.2012.

Wallace, Gregory K (1992). “The JPEG still picture compression standard”. In: *IEEE transactions on consumer electronics* 38.1, pp. xviii–xxxiv.

Kapany, Narinder S (1960). “Fiber optics”. In: *Scientific American* 203.5, pp. 72–81.

Kapany, NS and JJ Burke (1961). “Fiber optics. IX. Waveguide effects”. In: *JOSA* 51.10, pp. 1067–1078.

Agrawal, Govind P (2000). “Nonlinear fiber optics”. In: *Nonlinear Science at the Dawn of the 21st Century*. Springer, pp. 195–211.

Corning SMF 28 Ultra Optical Fiber (2014). PI1424. Corning.

Lefevre, HC (1980). “Single-mode fibre fractional wave devices and polarisation controllers”. In: *Electronics Letters* 16.20, pp. 778–780.

Kach, Alfred (1979). *Fiber optic T-coupler*.

Tomlinson III, Walter John (1978). *Wavelength division multiplexer*.

DiDomenico, M (1972). “Material dispersion in optical fiber waveguides”. In: *Applied optics* 11.3, pp. 652–654.

Feynman, RP, RB Leighton, and M Sands (1964). “Lectures on Physics, Volume 2, pp. 6-8 to”. In:

Levenson, MD and N Bloembergen (1974). "Dispersion of the nonlinear optical susceptibility tensor in centrosymmetric media". In: *Physical Review B* 10.10, p. 4447.

Gould, R Gordon et al. (1959). "The LASER, light amplification by stimulated emission of radiation". In: *The Ann Arbor conference on optical pumping, the University of Michigan*. Vol. 15, p. 128.

Steinmeyer, Günter (2002). "A review of ultrafast optics and optoelectronics". In: *Journal of Optics A: Pure and Applied Optics* 5.1, R1.

Weiner, Andrew (2011). *Ultrafast optics*. Vol. 72. John Wiley & Sons.

Jones, David J, Scott A Diddams, Jinendra K Ranka, Andrew Stentz, Robert S Windeler, John L Hall, and Steven T Cundiff (2000). "Carrier-envelope phase control of femtosecond mode-locked lasers and direct optical frequency synthesis". In: *Science* 288.5466, pp. 635–639.

Becker, Philippe M, Anders A Olsson, and Jay R Simpson (1999). *Erbium-doped fiber amplifiers: fundamentals and technology*. Elsevier.

Gruner-Nielsen, Lars, Marie Wandel, Poul Kristensen, Carsten Jorgensen, L Vilbrad Jorgensen, Bent Edvold, Bera Pálsdóttir, and Dan Jakobsen (2005). "Dispersion-compensating fibers". In: *Journal of Lightwave Technology* 23.11, pp. 3566–3579.

Mitra, Partha P and Jason B Stark (2001). "Nonlinear limits to the information capacity of optical fibre communications". In: *Nature* 411.6841, p. 1027.

Gui, Tao, Terence H Chan, Chao Lu, Alan Pak Tao Lau, and Ping-Kong Alexander Wai (2017). "Alternative decoding methods for optical communications based on nonlinear Fourier transform". In: *Journal of Lightwave Technology* 35.9, pp. 1542–1550.

Dispersion Compensating Fiber (2017). DCF38. Thorlabs.

Non-Zero Dispersion-Shifted Fiber (2018). TTN160391. Thorlabs.

Standard Highly Non-Linear Fiber Modules (2019). HNLF-ST. OFS.

Chmielak, Bartos, Michael Waldow, Christopher Matheisen, Christian Ripperda, Jens Bolten, Thorsten Wahlbrink, Michael Nagel, Florian Merget, and Heinrich Kurz (2011). "Pockels effect based fully integrated, strained silicon electro-optic modulator". In: *Optics express* 19.18, pp. 17212–17219.

Winzer, Peter J and Rene-Jean Essiambre (2008). "Advanced optical modulation formats". In: *Optical Fiber Telecommunications VB*. Elsevier, pp. 23–93.

Weis, RS and TK Gaylord (1985). "Lithium niobate: summary of physical properties and crystal structure". In: *Applied Physics A* 37.4, pp. 191–203.

Stobrawa, G, M Hacker, Th Feurer, D Zeidler, M Motzkus, and F Reichel (2001). “A new high-resolution femtosecond pulse shaper”. In: *Applied Physics B* 72.5, pp. 627–630.

Stroud, Jasper R and Mark A Foster (2019). “Ultrahigh-speed spatial pattern projection using a nonlinear optical time lens for fast single-pixel imaging”. In: *CLEO: Applications and Technology*. Optical Society of America, JW2A–79.

Wang, Ke-Yao and Amy C Foster (2012). “Ultralow power continuous-wave frequency conversion in hydrogenated amorphous silicon waveguides”. In: *Optics letters* 37.8, pp. 1331–1333.

Salem, Reza, Mark A Foster, and Alexander L Gaeta (2013). “Application of space–time duality to ultrahigh-speed optical signal processing”. In: *Advances in Optics and Photonics* 5.3, pp. 274–317.

Kolner, Brian H and Moshe Nazarathy (1989). “Temporal imaging with a time lens”. In: *Optics letters* 14.12, pp. 630–632.

Petrillo, Keith G and Mark A Foster (2011). “Scalable ultrahigh-speed optical transmultiplexer using a time lens”. In: *Optics express* 19.15, pp. 14051–14059.

Stroud, Jasper R, Olukayode Okusaga, Gregory Weaver, Nelli Mosavi, and Mark A Foster (2018). “Passive timing stabilization over a 33-km single mode fiber link using temporal imaging”. In: *2018 6th IEEE International Conference on Wireless for Space and Extreme Environments (WiSEE)*. IEEE, pp. 137–140.

Marcellin, Michael W, Michael J Gormish, Ali Bilgin, and Martin P Boliek (2000). “An overview of JPEG-2000”. In: *Proceedings DCC 2000. Data Compression Conference*. IEEE, pp. 523–541.

Landau, HJ (1967). “Sampling, data transmission, and the Nyquist rate”. In: *Proceedings of the IEEE* 55.10, pp. 1701–1706.

Donoho, David L et al. (2006). “Compressed sensing”. In: *IEEE Transactions on information theory* 52.4, pp. 1289–1306.

Eldar, Yonina C and Gitta Kutyniok (2012). *Compressed sensing: theory and applications*. Cambridge University Press.

Duarte, Marco F, Mark A Davenport, Dharmpal Takhar, Jason N Laska, Ting Sun, Kevin F Kelly, and Richard G Baraniuk (2008). “Single-pixel imaging via compressive sampling”. In: *IEEE signal processing magazine* 25.2, pp. 83–91.

Candès, Emmanuel J and Michael B Wakin (2008). “An introduction to compressive sampling [a sensing/sampling paradigm that goes against the common knowledge in data acquisition]". In: *IEEE signal processing magazine* 25.2, pp. 21–30.

Figueiredo, Mário AT, Robert D Nowak, and Stephen J Wright (2007). "Gradient projection for sparse reconstruction: Application to compressed sensing and other inverse problems". In: *IEEE Journal of selected topics in signal processing* 1.4, pp. 586–597.

Chapter 2

High speed optical coherence tomography using real time compression to achieve 28.8 MHz A-scan rates

2.1 Introduction

Over the past decade, optical coherence tomography (OCT) has proven to be an invaluable tool in medical diagnostics, allowing straightforward assessment of the progress of macular degeneration, multiple sclerosis, and glaucoma (Fercher et al., 2003; Tomlins and Wang, 2005). The massive amount of data collected in an OCT acquisition poses a problems in data storage and manipulation, requiring compression prior to any data processing (Zhang and Kang, 2010; Grulkowski et al., 2009). Additionally, in many applications the data acquisition needs to be done quickly to avoid motion artifacts that can distort the image (Yun et al., 2004; Zhang et al., 2009). Without the need for a scanning reference arm, spectral domain OCT (SD-OCT) techniques have increased A-scan rates from a few kHz to a few MHz (Leitgeb, Hitzenberger, and Fercher, 2003; Choi et al., 2012) by using CCD or CMOS cameras to sample and digitize the spectral interference. However, techniques that utilize cameras face limitations from the electronic data readout rate, as well as motion blur due to exposure time (Leitgeb et al., 2003). To avoid using cameras, swept source OCT techniques using Fourier domain mode locked (FDML) sources and dispersed supercontinuum sources have been used to produce a frequency mapped temporal signal that can be sampled with a single ADC (Huber et al., 2007; Moon and Kim, 2006). The use of mode locked lasers (MLL) and optical dispersion have become the state of the art in terms of speed, demonstrating A-scan rates from 7.14 MHz to 90.9 MHz (Xu et al., 2014; Goda et al., 2012). However, CCD/CMOS cameras, swept source methods, and dispersed MLL methods all read out the spectral interference signal serially using different methods of parallel to serial conversion. This introduces a hard limit on the total pixel rate of the OCT system to the speed of available ADC technology.

Information theory introduced compressed sensing (CS) (Candes and Tao, 2005; Candès, Romberg, and Tao, 2006; Donoho, 2006; Baraniuk, 2007; Candès and Wakin, 2008), suggesting natural sparsity can be leveraged to reduce the number of samples required to collect signals. This has been adopted by the medical field and applied to MRI imaging, photoacoustic imaging, and OCT (Lustig, Donoho, and Pauly, 2007; Guo et al., 2010; Liu and Kang, 2010). Particularly, Dr. Jin Kang's group has done extensive work on under sampling OCT data then implementing CS algorithms achieving successful reconstruction with less than 20% of measurements required by the Shannon/Nyquist theory

(Liu and Kang, 2010; Xu, Huang, and Kang, 2014). By taking advantage of the compressibility of volumetric OCT data due to sparsity in some domain (Wu et al., 2013), the data cube can be under sampled without the loss of image quality (Young et al., 2011). However many of these method still require the entire data cube to be recorded where the compression is applied after acquisition (Liu and Kang, 2010; Xu, Huang, and Kang, 2014; Wu et al., 2013; Young et al., 2011). Although compressed sensing after data acquisition allows for real time visualization, it fails to address the bottleneck due to serial readout on a single ADC.

We have previously implemented CS in the sampling stage of a high-speed microscope, ultra wide-band radio frequency (RF) sensing, and initial results in OCT (Bosworth et al., 2015b; Bosworth et al., 2015a; Stroud et al., 2016). Preliminary investigations into CS OCT system investigated the compressibility of A-scan and B-scan images (Stroud et al., 2016; Mididoddi et al., 2017). In this paper we present a system that utilizes compressed sensing in the axial dimension of the detected OCT signal and reconstructions the volumetric C-scan data utilizing transverse and depth sparsity. Taking advantage of CS theory, we sample inner products between the interference signals and know binary patterns such that each measurement contains information spanning the entire depth profile. This allows for real time photonic compression of the data prior to detection by a high speed ADC. We can remove the direct limit imposed by Nyquist sampling on A-scan rates, further extending the possibilities of high speed OCT.

2.2 Experiment

2.2.1 CS source

The optical source we developed for acquiring compressed measurements has been coined continuous high-rate photonically-enabled compressed sensing (CHiRP-CS) (Bosworth et al., 2015a). We use dispersion in optical fiber to directly modulate the spectrum of individual laser pulses. The principle for the CHiRP-CS source is shown in Fig. 1, using optical fiber and an electroptic modulator (EOM) the output laser pulses are modulated with unique binary spectral patterns.

The broadband laser source at 1550 nm and native 90 MHz repetition rate is multiplexed twice up to 360 MHz. The pulse train is then sent through 853 ps/nm dispersion optical fiber module to spread the 22 nm of optical bandwidth over 20 ns. This resulting frequency to time mapping allows the spectrum of the laser pulses to be modulated in time with an EOM operating at 11.52 Gb/s using a programed pseudorandom binary sequence (PRBS).

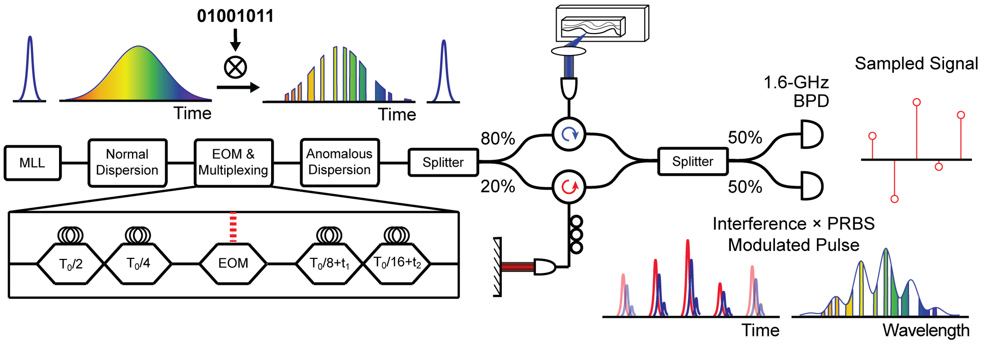

Figure 2.1: The dispersed and multiplexed MLL is modulated then recompressed to generate our CHiRP-CS source, which is sent into an OCT system. The sampled pulses are compressed measurements of the OCT interferogram.

With the 2.77 ns repetition cycle and over 20 ns pulse duration, neighboring pulses overlapped greatly, resulting in up to three pulses to be modulated simultaneously on different portions of their spectrum. Modulating the 360 MHz pulse source at 11.52 Gb/s results in sequential pulses spectrally shifting the PRBS pattern by 32 bits. In order to reach our final 1.44 GHz repetition rate, the patterned source is multiplexed twice more, with large delays of 166 ns and 306 ns. The dispersed pulses are recompressed in 50 km of SMF resulting in distinct pulses with unique spectral patterns at a 1.44 GHz pulse rate. We achieve spectral features of 12.53 GHz, over almost 3 THz of optical bandwidth, determined by the dispersive frequency to time mapping and EOM modulation rate.

In comparison with other work in CS OCT (Mididoddi et al., 2017), we disperse, modulate, and compress our pulses prior to entering the OCT interferometer, minimizing the losses in the EOM, optical fiber, and allowing for multiplexing after modulation. We are able to reach near the limit for the efficiency of our CS system, in terms of unique CS bits per second per nanometer.

2.2.2 OCT system

The OCT interferometer is set up with a mirror as a reference arm and a two-dimensional laterally scanning sample arm with a single 7.5 mm lens. The input CHiRP-CS source is split by a 80/20 couple where 80 percent enters the sample arm and 20 percent reaches the reference then are recombined in a 50/50 coupler then balanced detected by a 1.6 GHz amplified photodetector.

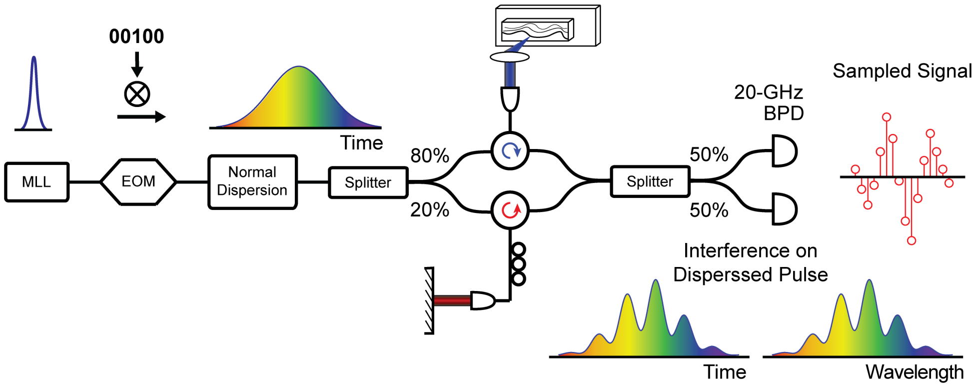

Figure 2.2: The dispersed and pulse picked MLL is sent into an OCT system. The interferogram on the dispersed pulses are directly sampled by a high speed detector.

The signal is digitized by a 20 GHz 40 GS/s oscilloscope and read out to a computer for data processing and image reconstruction. When the CHiRP-CS source returns from the interferometer the pulse spectrum is modulated by the interference between the reference arm and the sample. As illustrated in Fig. 1 a single sample of the pulse amplitude contains information spanning the entire spectrum, the inner product between the interference signal and the binary pattern.

In order to investigate the fidelity of our CS approach, we also acquire a AOT-OCT measurement in series with our CS measurement (Xu et al., 2014; Goda et al., 2012). As shown in Fig. 2, the 90 MHz MLL is sent into an EOM to be pulse picked down to 18 MHz, necessary to avoid pulse overlap after the pulses then propagate through 853 ps/nm dispersion module to achieve sufficient frequency to time mapping for comparable resolution to our CS system. This signal is balanced detected by a 20 GHz linear photodetector, then digitized by a 20 GHz 40 GS/s oscilloscope. The range and roll-off of the OCT system is shown inset in Fig. 2, demonstrating a 5 dB/mm loss of signal power when the reference mirror is shifted in the axial direction.

2.3 Results

2.3.1 CS reconstruction

To scan a three-dimensional(3−D) object $\boldsymbol{S}$ of size $N_1 \times N_2 \times N_3$, we generate $N_1 \times N_2$ number of measurements for a C-scan, with each measurement of length M. Let $\boldsymbol{y}^{(i,j)} \in \mathbb{R}^M, i = 1, 2, ..., N_1, j = 1, 2, ..., N_2$ denotes the measurements vector collected from the signal at a spatial location $(i, j) : \boldsymbol{s}^{(i,j)}$, and $\boldsymbol{A}^{(i,j)} \in \mathbb{R}^{M \times N_3}$ is the sensing matrix associated with that measurement. The mathematical model of the system is simply:

$$\boldsymbol{y}^{(i,j)} = \boldsymbol{A}^{(i,j)} \boldsymbol{s}^{(i,j)} + \boldsymbol{z}^{(i,j)}, \tag{2.1}$$

where $\boldsymbol{z}^{(i,j)}$ represents the noise vector added to the (i, j)-th noiseless measurement from multiple sources that create noise such as the linearization approximation error of the system, noise from the data collection process, as well as pre-processing error, etc.

Due to the system setting, the frequencies correspond to different depths of the object. Here, the sensing object: microscope slip has a few layers, resulting a small number of cosine tones along the direction that the system takes measurement (A-scan direction). Therefore, if we represent the signal using discrete Fourier basis, we would expect the coefficients corresponding to that basis to be sparse. Accordingly, we utilize sparsity with respect to the inverse discrete Fourier transform in the recovery algorithm. The noise of the system is high frequency. Consequently, the high frequency parts of the signal become less distinguishable from the noise. While applying sparse recovery with the classic ℓ_1 min norm, we observe that as the sparsity level λ is increasing, the power of the high frequency part vanishes much faster than the low frequency part. As a result, certain depth of the object is almost complete missing. To resolve this issue, we employ a weighted ℓ_1 minimization. Similar treatment is proposed in (Khajehnejad et al., 2009).

For non-negative weights $w_i \geq 0, \boldsymbol{w} = (w_1, w_2, ..., w_{N_3})$, the weighted $\ell_{\boldsymbol{w},1}$ norm of vector $\boldsymbol{x}$ is defined as $\|\boldsymbol{x}\|_{\boldsymbol{w},1} = \sum_{i=1}^{N_3} w_i |x_i|$. For variable matrix $\boldsymbol{X} = (\boldsymbol{x}^{(1)}, \boldsymbol{x}^{(2)}, ..., \boldsymbol{x}^{(N_1 N_2)})$, we find:

$$\widetilde{\boldsymbol{X}} = arg\,min_{\boldsymbol{X} \in \mathbb{C}^{N_3 \times N_1 N_2}} \frac{1}{2} \sum_{k=1}^{N_1 N_2} \|\boldsymbol{y}^{(k)} - \boldsymbol{A}^{(k)} \boldsymbol{\Phi} \boldsymbol{x}^{(k)}\|_2^2 + \lambda \sum_{k=1}^{N_1 N_2} \|\boldsymbol{x}^{(k)}\|_{\boldsymbol{w},1}, \quad (2.2)$$

where the sparisfying transform $\boldsymbol{\Phi}$ is the inverse discrete Fourier basis. The non-negative regularization parameter $\lambda > 0$ balances the ratio of sparsity of the solution and the fitness of the solution respect to the measurements. The larger value of λ leads to a more sparse solution. The equation (2.2) is initialized by solving the regular ℓ_1 minimization problem:

$$\widetilde{\boldsymbol{X}_0} = arg\,min_{\boldsymbol{X}_0 \in \mathbb{C}^{N_3 \times N_1 N_2}} \frac{1}{2} \sum_{k=1}^{N_1 N_2} \|\boldsymbol{y}^{(k)} - \boldsymbol{A}^{(k)} \boldsymbol{\Phi} \boldsymbol{x}^{(k)}\|_2^2 + \lambda_0 \sum_{k=1}^{N_1 N_2} \|\boldsymbol{x}_0^{(k)}\|_1, \quad (2.3)$$

where $\|\boldsymbol{x}\|_1$ calculate the sum of absolute values of all entries of $\boldsymbol{x} : \|\boldsymbol{x}\|_1 = \sum_{i=1}^{N_3} |x_i|$. and the weight $\boldsymbol{w}$ in Eq. (2.2) is a function associated with the power spectrum of $\widetilde{\boldsymbol{X}_0}$. More details is explained in the Section 2.3.2.

The above two optimization problems can be solved efficiently by several methods such as iterative methods (Combettes and Wajs, 2005; Beck and Teboulle, 2009), gradient projection (Figueiredo, Nowak, and Wright, 2007), alternating minimization (Boyd et al., 2011), approximate message passing (Donoho, Maleki, and Montanari, 2009), etc. In our implementation, we use gradient projection for sparse reconstruction (Figueiredo, Nowak, and Wright, 2007).

2.3.2 Experimental Results

To visualize the reconstruction result, we calculate the 3−D power spectrum of the recovered signal as the following: the magnitude for each discrete frequency from $\widetilde{X}$ is calculated by summing the squared coefficients of positive and negative frequencies corresponding location.

The 3−D view of the power spectrum of the reference signal is shown

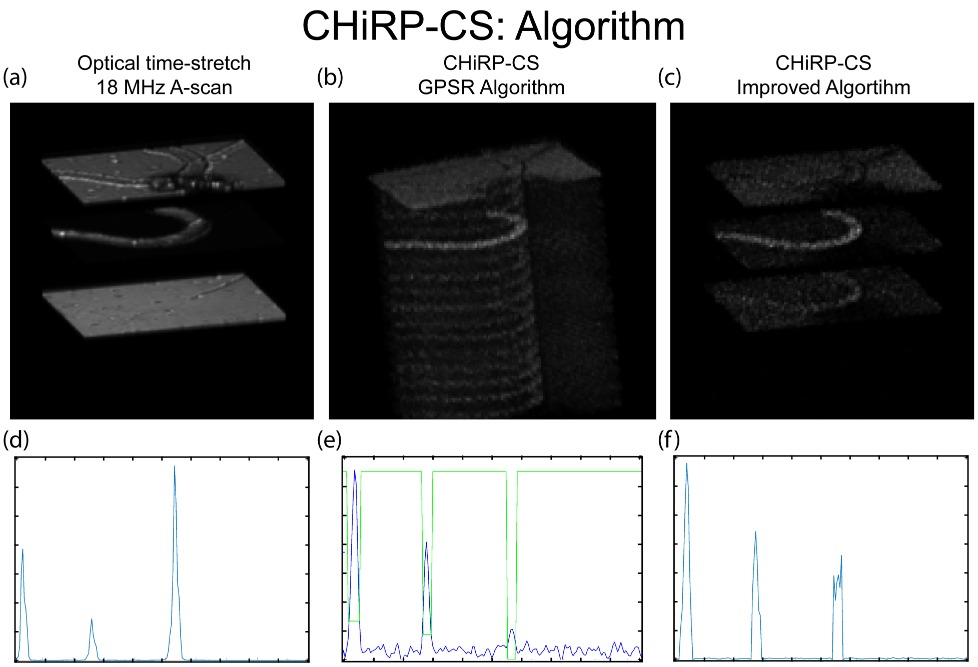

Figure 2.3: Recovery from 50 sequential measurements per A-scan. The top row: 3−D power spectrum and the bottom row: 1-D power spectrum. The ground truth a), d) or the raster scanning technique, compared to b), e) the GPSR compressed reconstruction algorithm, and c), f) our improved CS algorithm showing noise reduction.

in Fig. 3a, in which from top to bottom, different locations correspond to low frequencies to high frequencies. The power spectrum of the reference signal shows the shape of the actual object, an empty PDMS microfluidic channel mounted on a glass slide. We then sum up the power values along each slice that have correspond to the same frequency in different geometric locations to obtain a $1-$D spectrum statistics, which is depicted in Fig. 3d.

The initialization from ℓ_1 minimization is displayed in Fig 3b. The solution from ℓ_1 minimization detects the frequencies of the signal relatively accurately however we lose a lot of energy in the high frequency bands. Also, the energy for the middle slice with curved line pattern is aliased to higher frequency bands.

The $1-$D power spectrum statistic is shown in Fig. 3e and we will use it to determine the weights for weighted ℓ_1 minimization algorithm to resolve those issues. First we search for peaks from ℓ_1 minimization solution to determine the support and non-support part of the signal. We use three parameters to determine the peaks: the lowest energy with ratio $\tau \in [0, 1]$ that are non-support part of the signal based on sparsity assumption, the minimum width $\delta \in \mathbb{Z}^+$ to be a strong peak, and minimum peak radius from peak boundaries to local maximum (peak centers) $\rho \in \mathbb{Z}^+$. In our experiment, we pick $\tau = 85\%, \delta = 3, \rho = 2$. We eliminate the support locations based on the first two parameters. For the detected peaks, we find the local maximum within each local region, treat it as the peak center and extend its boarder to 2ρ if the boarder to center distance is less than ρ, encouraging a smoother transaction between support and non-support part in the solution. Then we generate the weight function $\boldsymbol{w}$ according to the result from peak detection.

The square root of the averaged power within each peak region are used as weights. For the non-support part, we set the weights w_i to be 2 times the square root of the max value of the $1-$D power spectrum vector. The green line in Fig. 3e shows the weights assigned to each location of the half of the sparse code. The higher the weight, the magnitude of corresponding location tends to be zero because the weight contributes more to the penalty. All parameters in peak finding function and weight function are determined empirically and this choice of weight function will make the value of non-support part smaller and boost the energy of high frequency bands. The resulting $1-$D power spectrum is depicted in Fig. 3f.

We could see that the energy of the non-support portion detected by the algorithm decreases significant and the magnitude of the high frequency part of the signal is boosted. Although it introduces some non-smoothness for the $1-$D spectrum of the signal, there is no visible non-smooth region in the recovered $3-$ D spectrum.

We could see in Fig 4a, when the number of measurements increases, the algorithm is able to recover more details of the signal and the reconstruction result is improved. Fig. 4b and Fig 4c illustrate the reconstruction result from 50 and 100 measurements randomly selected from all measurements per A-scan direction respectively measured by Peak Signal-to-Noise Ratio (PSNR). This is analogous with changing the multiplexing such that all the stages are after the modulator with some delay. We could see that for the same amount of measurements, randomly selected one has less aliasing in the high frequency by comparing Fig 3b and Fig 4b.

We compare the reference Nyquist sampled AOT measurement of the

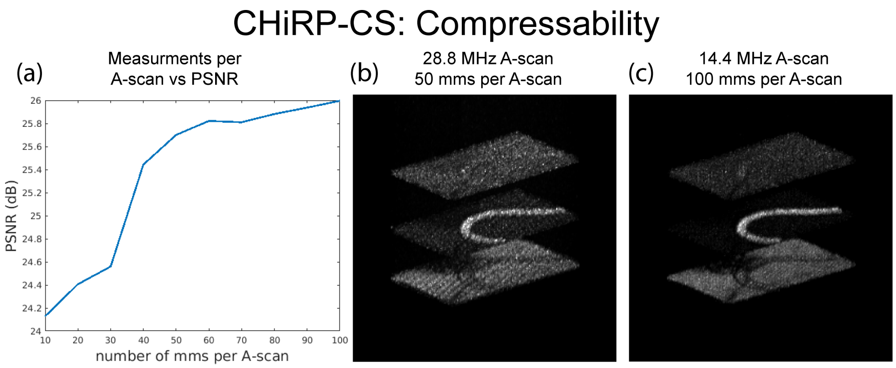

Figure 2.4: The PSNR of the CS reconstruction vs the number of compressed measurements used a) shows an increase in PSNR around b) 50 measurements and we see a slight improvement using c) 100 measurements.

section of microfluidic channel to our CS reconstructions in Fig. 4(b,c). The ground truth image in Fig 3a shows three distinct layers, representing the air-glass interface, the glass-PDMS interface, and PDMS-air interface from bottom to top, or low to high frequencies respectively. The PDMS-glass low contrast interface is interrupted by the air gap channel which is smaller than the axial resolution of the system, creating the clear channel in the center layer of the image. The CHiRP-CS reconstructions are shown at different compression ratios, showing reconstructions with normal and random sampling, top and bottom respectively. We can reconstruct the microfluidic channel with only 13% of the samples required by Nyquist, a 28.8 MHz A-scan rate. We also show the image at 26% compression or 14.4 MHz A-scan shows a reduction in noise and reconstruction artifacts. The random sampling improves the reconstruction further, almost eliminating the artifacts, as well as reducing the noise power in the middle layer outside of the channel. The 18 MHz

A-scan rate achieved with AOT requires a detector a decade faster and takes four times longer to complete an A-scan compared to our 13% CHiRP-CS reconstructions.

2.4 Conclusion

In this paper we present a compressed sensing OCT system that both address the need for high speed data acquisition and offers a solution to the complications large volumetric data causes for storage and processing. We show real-time compression of the OCT signals, allowing for far fewer measurements needed to complete an A-scan, resulting in faster collection times. Going further than previous work in CS OCT, we show the potential to leverage sparsity in both axial and transverse direction to reconstruct full C-scan data cube. We show successful reconstruction with under a third of the measurements required by Nyquist sampling, achieving up to a 28.8 MHz A-scan rate. These results suggest that the limit on pixel rate imposed by the ADC technology can be surpassed to expand the impact of OCT systems.

References

Fercher, Adolf F, Wolfgang Drexler, Christoph K Hitzenberger, and Theo Lasser (2003). “Optical coherence tomography-principles and applications”. In: *Reports on progress in physics* 66.2, p. 239.

Tomlins, Peter H and RK Wang (2005). “Theory, developments and applications of optical coherence tomography”. In: *Journal of Physics D: Applied Physics* 38.15, p. 2519.

Zhang, Kang and Jin U Kang (2010). “Real-time 4D signal processing and visualization using graphics processing unit on a regular nonlinear-k Fourier-domain OCT system”. In: *Optics express* 18.11, pp. 11772–11784.

Grulkowski, Ireneusz, Michalina Gora, Maciej Szkulmowski, Iwona Gorczynska, Daniel Szlag, Susana Marcos, Andrzej Kowalczyk, and Maciej Wojtkowski (2009). “Anterior segment imaging with Spectral OCT system using a high-speed CMOS camera”. In: *Optics express* 17.6, pp. 4842–4858.

Yun, Seok H, Guillermo J Tearney, JF de Boer, and BE Bouma (2004). “Pulsed-source and swept-source spectral-domain optical coherence tomography with reduced motion artifacts”. In: *Optics Express* 12.23, pp. 5614–5624.

Zhang, Kang, Weichao Wang, Jaeho Han, and Jin U Kang (2009). “A surface topology and motion compensation system for microsurgery guidance and intervention based on common-path optical coherence tomography”. In: *IEEE Transactions on Biomedical Engineering* 56.9, pp. 2318–2321.

Leitgeb, R, CK Hitzenberger, and Adolf F Fercher (2003). “Performance of fourier domain vs. time domain optical coherence tomography”. In: *Optics express* 11.8, pp. 889–894.

Choi, Dong-hak, Hideaki Hiro-Oka, Kimiya Shimizu, and Kohji Ohbayashi (2012). “Spectral domain optical coherence tomography of multi-MHz A-scan rates at 1310 nm range and real-time 4D-display up to 41 volumes/second”. In: *Biomedical optics express* 3.12, pp. 3067–3086.

Leitgeb, Rainer A, L Schmetterer, W Drexler, AF Fercher, RJ Zawadzki, and T Bajraszewski (2003). “Real-time assessment of retinal blood flow with ultrafast acquisition by color Doppler Fourier domain optical coherence tomography". In: *Optics Express* 11.23, pp. 3116–3121.

Huber, R, DC Adler, VJ Srinivasan, and JG Fujimoto (2007). "Fourier domain mode locking at 1050 nm for ultra-high-speed optical coherence tomography of the human retina at 236,000 axial scans per second". In: *Optics letters* 32.14, pp. 2049–2051.

Moon, Sucbei and Dug Young Kim (2006). "Ultra-high-speed optical coherence tomography with a stretched pulse supercontinuum source". In: *Optics Express* 14.24, pp. 11575–11584.

Xu, Jingjiang, Chi Zhang, Jianbing Xu, KKY Wong, and KK Tsia (2014). "Megahertz all-optical swept-source optical coherence tomography based on broadband amplified optical time-stretch". In: *Optics letters* 39.3, pp. 622–625.

Goda, Keisuke, Ali Fard, Omer Malik, Gilbert Fu, Alan Quach, and Bahram Jalali (2012). "High-throughput optical coherence tomography at 800 nm". In: *Optics express* 20.18, pp. 19612–19617.

Candes, Emmanuel J and Terence Tao (2005). "Decoding by linear programming". In: *IEEE transactions on information theory* 51.12, pp. 4203–4215.

Candès, Emmanuel J, Justin Romberg, and Terence Tao (2006). "Robust uncertainty principles: Exact signal reconstruction from highly incomplete frequency information". In: *IEEE Transactions on information theory* 52.2, pp. 489–509.

Donoho, David L (2006). "Compressed sensing". In: *IEEE Transactions on information theory* 52.4, pp. 1289–1306.

Baraniuk, Richard G (2007). "Compressive sensing [lecture notes]". In: *IEEE signal processing magazine* 24.4, pp. 118–121.

Candès, Emmanuel J and Michael B Wakin (2008). "An introduction to compressive sampling". In: *IEEE signal processing magazine* 25.2, pp. 21–30.

Lustig, Michael, David Donoho, and John M Pauly (2007). "Sparse MRI: The application of compressed sensing for rapid MR imaging". In: *Magnetic Resonance in Medicine: An Official Journal of the International Society for Magnetic Resonance in Medicine* 58.6, pp. 1182–1195.

Guo, Zijian, Changhui Li, Liang Song, and Lihong V Wang (2010). "Compressed sensing in photoacoustic tomography in vivo". In: *Journal of biomedical optics* 15.2, p. 021311.

Liu, Xuan and Jin U Kang (2010). "Compressive SD-OCT: the application of compressed sensing in spectral domain optical coherence tomography". In: *Optics express* 18.21, pp. 22010–22019.

Xu, Daguang, Yong Huang, and Jin U Kang (2014). “Volumetric (3D) compressive sensing spectral domain optical coherence tomography”. In: *Biomedical optics express* 5.11, pp. 3921–3934.

Wu, Andy Bo, Evgeniy Lebed, Marinko V Sarunic, and Mirza Faisal Beg (2013). “Quantitative evaluation of transform domains for compressive sampling-based recovery of sparsely sampled volumetric OCT images”. In: *IEEE Transactions on Biomedical Engineering* 60.2, pp. 470–478.

Young, Mei, Evgeniy Lebed, Yifan Jian, Paul J Mackenzie, Mirza Faisal Beg, and Marinko V Sarunic (2011). “Real-time high-speed volumetric imaging using compressive sampling optical coherence tomography”. In: *Biomedical optics express* 2.9, pp. 2690–2697.

Bosworth, Bryan T, Jasper R Stroud, Dung N Tran, Trac D Tran, Sang Chin, and Mark A Foster (2015b). “Ultrawideband compressed sensing of arbitrary multi-tone sparse radio frequencies using spectrally encoded ultrafast laser pulses”. In: *Optics letters* 40.13, pp. 3045–3048.

Bosworth, Bryan T, Jasper R Stroud, Dung N Tran, Trac D Tran, Sang Chin, and Mark A Foster (2015a). “High-speed flow microscopy using compressed sensing with ultrafast laser pulses”. In: *Optics express* 23.8, pp. 10521–10532.

Stroud, Jasper R, Bryan Bosworth, Dung Tran, Trac D Tran, Sang Chin, and Mark A Foster (2016). “72 MHz A-scan optical coherence tomography using continuous high-rate photonically-enabled compressed sensing (CHiRP-CS)”. In: *CLEO: Science and Innovations*. Optical Society of America, SM2I–1.

Mididoddi, Chaitanya K, Fangliang Bai, Guoqing Wang, Jinchao Liu, Stuart Gibson, and Chao Wang (2017). “High-Throughput Photonic Time-Stretch Optical Coherence Tomography with Data Compression”. In: *IEEE Photonics Journal* 9.4, pp. 1–15.

Khajehnejad, M Amin, Weiyu Xu, A Salman Avestimehr, and Babak Hassibi (2009). “Weighted l-1 minimization for sparse recovery with prior information”. In: *Information Theory, 2009. ISIT 2009. IEEE International Symposium on*. IEEE, pp. 483–487.

Combettes, Patrick L and Valérie R Wajs (2005). “Signal recovery by proximal forward-backward splitting”. In: *Multiscale Modeling & Simulation* 4.4, pp. 1168–1200.

Beck, Amir and Marc Teboulle (2009). “A fast iterative shrinkage-thresholding algorithm for linear inverse problems”. In: *SIAM journal on imaging sciences* 2.1, pp. 183–202.

Figueiredo, Mário AT, Robert D Nowak, and Stephen J Wright (2007). “Gradient projection for sparse reconstruction: Application to compressed sensing and other inverse problems”. In: *IEEE Journal of selected topics in signal processing* 1.4, pp. 586–597.

Boyd, Stephen, Neal Parikh, Eric Chu, Borja Peleato, Jonathan Eckstein, et al. (2011). “Distributed optimization and statistical learning via the alternating direction method of multipliers”. In: *Foundations and Trends® in Machine learning* 3.1, pp. 1–122.

Donoho, David L, Arian Maleki, and Andrea Montanari (2009). “Message-passing algorithms for compressed sensing”. In: *Proceedings of the National Academy of Sciences* 106.45, pp. 18914–18919.

Chapter 3

Optical time-lens spectral shaper for high speed single-pixel imaging

3.1 Introduction

The ability to record images at a moments notice has become essential in everday life. The widespread use of CCD and CMOS camera has not only revolutionized communication and media, but medical image, materials science, and many others (Brynk et al., 2012; Huang et al., 2011). These cameras allow us to record the response of visible light, and convert it into a digital form at ever increasing speeds, pixel number, and density. Today, we have high speed camera that reach up to a few Megaframes per second, and high resolution cameras with hundreds of megapixels (*H6D-400C MS* 2019; *the world's most versatile family of high speed camera systems!* 2019). However, with this technology comes two setbacks, first being the limited wavelength response of these silicon CCDs, and second the tradeoff between high-speed and pixel number due to the serial digital readout.

Although technology inside CCD cameras has improved steadily, the core technology of silicon detectors has a limited wavelength response. Other materials used for non-visible light has proved difficult, with only bulky, power consuming equipment available (Tonouchi, 2007; Onaka et al., 2007). This has made it difficult for many applications in science and industry, where material interaction occur in a different wavelength range (Oh et al., 2006). Secondly, the digital readout of any detector based device is done serially, meaning each pixel is read out one at a time. This provides a maximum limit for how fast a certain amount of pixels can be generated by a camera, limiting either the frame rate, or resolution of the image (*the world's most versatile family of high speed camera systems!* 2019; Grulkowski et al., 2009). The process of making photo-receptive cells smaller, faster, and broader bandwidth can only go so far in improve camera technology. With the limits of traditional cameras are known very well, more exotic architectures are being investigated (Slyper, Poupyrev, and Hodgins, 2011; Song et al., 2013). While different camera array configurations provide some benefit, they all rely on the same Nyquist sampling theory that limits total information sensing of the system.

Single-pixel imaging systems using compressed sensing (CS) have shown the ability to capture images with far fewer samples than traditionally required by the Nyquist-Shannon sampling theorem (Donoho et al., 2006; Eldar and Kutyniok, 2012). Information theory tells us that naturally images can be represented in some mathematical basis where the signal is very sparse. This allows modern compression such as JPEG and JPEG-2000, allowing the storing of information to be far smaller than the collected data (Wallace, 1992; Marcellin et al., 2000). Further, the theory can be extended, where an image can be collected in a way such that it is already compressed, allowing for far fewer measurements to be taken. This can be realized using a single pixel camera architecture, where the systems collects inner products between the image and known patterns. As opposed to traditional Nyquist sampling, where information from only one pixel is collected and sampled individually, a single pixel measurement contains information throughout the entire image (Duarte et al., 2008).

Hardware implementations of a single pixel cameras have been implement with success, and extended to a variety of applications where traditional cameras are lacking (Chan et al., 2008; Welsh et al., 2013; Ma, 2009). However, these single-pixel imaging approaches are based on technologies that modulate light spatially (e.g. digital micromirror devices (DMDs) and spatial light modulators (SLMs)). Although these electronic devices are very flexible, they are generally extremely slow and operate at pattern rates below 20 kHz, limiting the frame rate of single pixel cameras to tens of Hz (Sun et al., 2016a; Sun et al., 2016b). The limitation of these systems is the rate at which the patterns can be programmed, not the number of samples that is ready out by a digitizer. Solutions to this have been presented using laser speckle or a coded aperture to generate multiple patterns simultaneously and collect then with parallel detectors (Shin, Bosworth, and Foster, 2016; Shin, Bosworth, and Foster, 2017). However, this is not a perfect solution, as it is simply spatially multiplexing a compressed measurement, the true limit is still how quickly the patterns can change. Solutions are needed to generate high speed patterns for single pixel camera architecture to maximize the collected information per second.

We have previously demonstrated the use of high-speed electro-optic spectral shaping for the compressive measurement of one-dimensional spectrally mapped spatial signals (Bosworth et al., 2015; Stroud et al., 2016). This approach was extended to two-dimensions, but the number of programmable image pixels was limited to only 320, creating a very small image frame (Guo et al., 2015). The limitation in image pixels results from the use of a chirp-processing and electro-optic modulation to generate the spectral patterns. Such a chirp-processing system is bandwidth inefficient requiring the use of much greater optical bandwidths than the signal bandwidth and thus limiting the number of features that can be measured with a given optical bandwidth (Bosworth et al., 2015; Stroud and Foster, 2017). Here we demonstrate two-dimensional pattern projection at and 3,212 pixels per pattern and 289 Gpixels/s using a four-wave mixing (FWM) time-lens based spectral shaper. In contrast to chirp-processing, a time-lens based system provides much higher bandwidth efficiency and thus can greatly increase the number of image pixels for a given optical bandwidth. Using this source, we demonstrate continuous two-dimensional single-pixel imaging at tens of kHz frame-rates and thousands of pixels per frame.

3.2 Experiment

3.2.1 Optical time lens spectral shaper

The operating principle of our spectral shaper is a parametric mixing based optical time lens (Stroud and Foster, 2017; Salem, Foster, and Gaeta, 2013).

Parametric mixing has terahertz of bandwidth, enabling a variety of communications and signal processing technology. An optical time lens is based on the analogous forms of diffraction and dispersion. Therefore, the spatial manipulation of an optical beam can be translated to an optical pulse. One of the more interesting effects of a lens is the ability to take a spatial Fourier transform of an image. Figure 1a shows the process of a lens transforming an image into the spatial Fourier domain, where a quadratic phase shift imparted by the glass lens is the transform mechanic. In order to achieve an analogous temporal Fourier transform, a quadratic phase shift needs to be applied to the pulse.

There are a few methods of applying a temporal quadratic phase shift. Electro-optic modulation can impart a sinusoidal waveform that can approximate a quadratic, but the limited total phase shift and limit the time lens performance. Parametric FWM allows for large phase shift and high-speed processing, using a chirped pump pulse (Salem, Foster, and Gaeta, 2013). The is due to the relationship between phase and frequency, where the phase is the derivative of frequency $\delta\phi = \delta f$, meaning a quadratic phase shift is a linear frequency shift. Figure 1a shows how a chirped pump pulse can impart a linear frequency shift on the generated idler. Four-wave mixing is the process where two pump photons generate a signal and idler photon through the $\chi^{(3)}$ nonlinearity. If the pump pulse is chirped, the frequency to time mapping results in a time dependent FWM interaction that imparts a linear frequency shift on the signal.

Analogous to how a lens can take a Fourier transform, a chirped pulse FWM time lens can take the temporal Fourier transform. In order to achieve a spatial transform, the image must be placed at the focal point of the lens, and the transformed image will be at the opposite focal point. Similarly, a time lens requires propagation in optical fiber equal to the focal point of the time lens, and then propagated back through the opposite dispersion to complete the transform. Using a degenerate FWM time lens as shown in Fig. 1a means the focal length of the time lens is half of the pump pulse dispersion, due to the additive nature of the phase imparted by the pump pulse.

To realize a FWM time lens, we use a 90-MHz mode locked laser (MLL) that is spectrally broadened and filtered to achieve a flat spectral profile over 8-nm of bandwidth. The ultrahigh-speed serial optical waveform is created from 1.2-ps pulses from a 10.08-GHz MLL that are modulated at 10.08 Gb/s with a pseudorandom bit sequence (PRBS) using an electro-optic modulator (EOM) and temporally multiplexed up to a final 322.56-GHz pulse rate. The 90-MHz (pump) and 322.56-GHz (signal) pulse trains are double passed through spools of standard single mode fiber (SMF) with 550 ps/nm and 275 ps/nm of dispersion respectively, using circulators and Faraday mirrors. The now dispersed pump and signal are amplified and combined before undergoing FWM in 700-m of highly nonlinear fiber (HNLF), where the pump applies the quadratic phase shift of the time-lens, converting the temporal profile of the input signal onto the spectrum of the FWM idler. The optical bandwidth and length of dispersive fiber determine the number and size of our features. In this system, the 8-nm pump pulse is stretched to over 8.8 ns, allowing for a spectral feature size of 730 MHz and over 3,000 features per pulse bandwidth. The FWM idler is filtered out, amplified, and compressed in dispersion compensating fiber (DCF) to produce optical pulses with unique

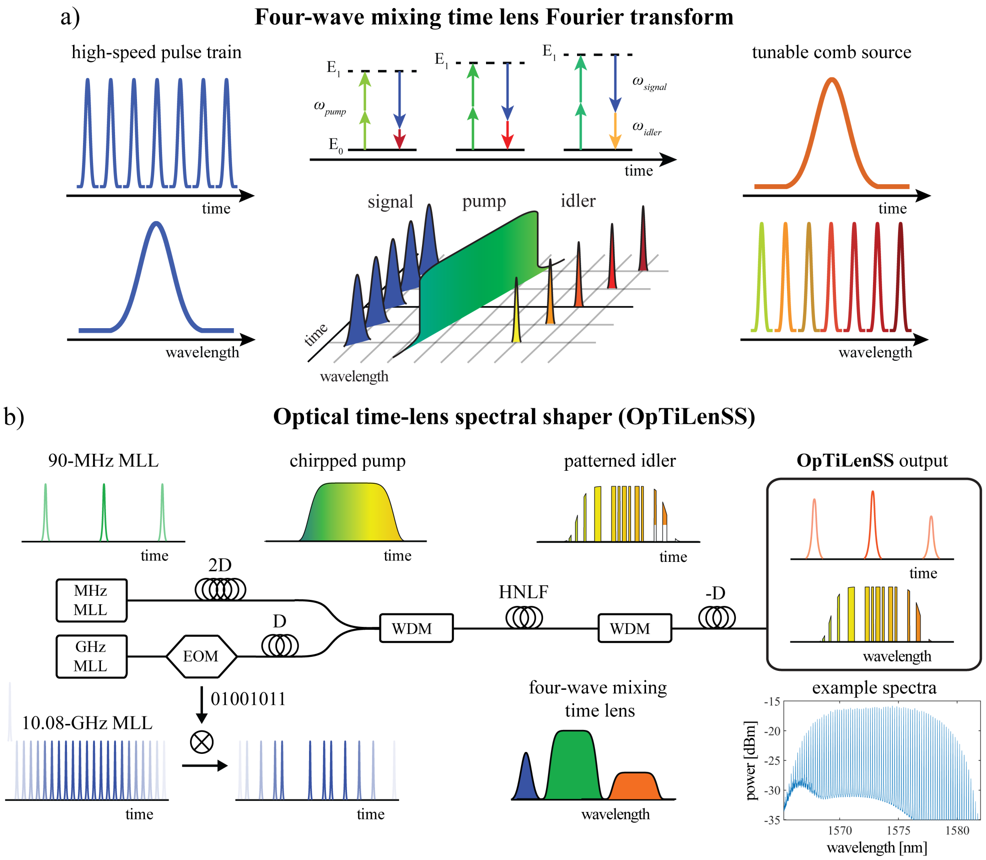

Figure 3.1: a) Using the analogous relation between spatial diffraction and temporal dispersion, we use a quadratic temporal phase shift to take the Fourier transform of a signal. The phase shift imparted by a chirped pump in green produces the idler in red, the Fouier transform of the signal in blue. b) By using a four-wave mixing time lens, we can generate high-resolution spectral patterns by transforming a high-speed pulse train. We us a 90-MHz MLL that is stretched in SMF by 1100 ps/nm and the 10.08-GHz MLL signal is dispersed by 550 ps/nm, or the focal length of the time lens. The two are mixed in HNLF and the output idler is filtered and sent through -550 ps/nm DCF to complete the transform. We can generate unique spectral patterns by modulating the signal with a PRBS at 10.08 Gb/s and multiplexing five times to achieve a final 322.56 Gb/s. MLL - mode-locked laser, EOM - electro-optic modulator, WDM - wavelength division multiplexer, SMF - single mode fiber, DCF - dispersive compensating fiber.

spectral patterns.

The full optical time lens spectral shaper (OpTiLenSS) system is shown in Fig 1b, where the high speed time domain signal is transformed into a high-resolution spectral pattern. The minimal spectral feature on the compressed output is defined by the duration $\tau pump$ of the transform limited pump pulse by $\tau_{res} = \frac{\tau_{pump}}{\sqrt{2}}$. The total length of the time lens also depends on the pump pulse bandwidth as well as the dispersion or focal length of the lens, defined as $D =$, where β_2 and L define the focal length and Ω_{pump} is the pump bandwidth. The temporal to spectral mapping shown in the insert in Fig 2 translates a 10.08 Gb/s modulation to a 23 GHz separation defined by,

$$\frac{\Delta t}{\Delta \omega} = |\beta_2 L| \tag{3.1}$$

With a final modulation rate of 322.56 GB/s generates 720 MHz spectral features. The total transformed duration is about 8.8 nanoseconds, meaning there are over 3000 spectral features per pulse. We use this large number of programable spectral bits for compressed sensing single pixel camera using a two-dimensional projector.

3.2.2 Two-dimensional spectral projector

The high-speed programable spectral shaper is combined with a two-dimensional spectral mapper to collect single-pixel camera measurements. The spectrally patterned laser pulses are mapped spatially using a diffraction grating and virtually imaged phased array (VIPA) (Xiao, Weiner, and Lin, 2004). The optical setup is shown in Fig. 2 where the input beam is focused into a line by a cylindrical lens, so it will enter the small VIPA entrance slit, where the different wavelengths are mapped spatially in the vertical direction. This type of interference based spatial mapping causes wavelengths separated by the free spectral range (FSR) of the VIPA, determined by the structure, to propagate out of the VIPA at the same angle. This results in a spectral mapping of each FSR vertically, which is followed by a diffraction grating to separate the different FSR horizontally. The output of the diffraction grating is sent through a focusing lens that forms an image of the spectral pattern on the object plane, with each wavelength projecting to a different spatial location over a two-dimensional grid.

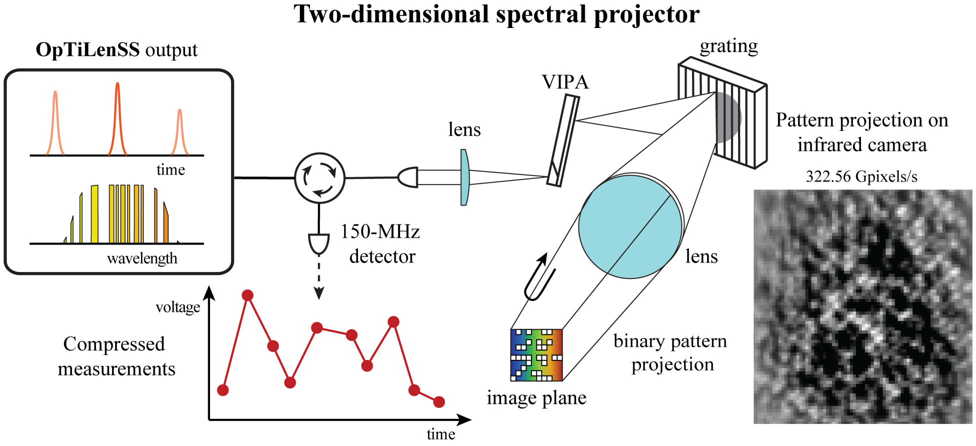

Figure 3.2: The two-dimensional spectral projection is done using a grating and VIPA to spread the spectrum out horizontally and vertically, respectively. The grating has 600 grooves per mm, and a 1.6-um blaze wavelength, while the VIPA has a 30 GHz FSR, resulting in our 73 by 44 projection over a 1.7 by 1.2 mm area. Using our OpTiLenSS source, we show an example pattern detected using an infrared camera, achieving a 322.56 Gpixels/s spectral projection.

The OpTiLenSS source pulses are collimated and focused into a line using a 50 cm cylindrical lens that travels through a VIPA with a 30 GHz FSR and diffraction grating with 600 grooves/mm and 1.6 um blaze wavelength. The vertical and horizontal mapping place each wavelength at a different spatial location, producing a projected pattern over a 1.7 by 1.2 mm area with 73 and 44 pixels respectively. An example pattern is shown in Fig. 2 on an infrared camera. The reflection from the object plane is returned through the two-dimensional spatial mapper and detected with a 150 MHz amplified photo-detector, where the power of each pulse in the 90 MHz pulse train represents the inner product between the object and the projected pattern. The pulse powers are sampled and digitized then processed by a reconstruction algorithm that converts the compressed measurements and known OpTiLenSS patterns into an image.

3.3 Results

3.3.1 Reconstruction algorithm

According to CS theory, a sparse signal of N length can be measured through a set of M such inner products, y = Ax, where A is an uncorrelated basis (i.e. the PRBS pattern set) by solving for x (the image of the object) in the minimization

$$\min ||W\hat{x} - \lambda||_1 \quad \dots \quad \textit{while } \boldsymbol{A}\hat{x} - y_{CS} = 0. \tag{3.2}$$

where W is a sparsifying matrix, and λ is a constant that bounds the reconstructed signal x to the measurements y = Ax. Through iterations of minimizing the number of active dictionary elements in Wx, the algorithm reconstructs the signal x by finding the sparest solution that satisfies the M « N pulse amplitude measurements y.

In order to enforce sparse image reconstruction, we take advantage of local image sparsity, similar to JPEG or JPEG2000. As shown in Fig. 3, the estimate image reconstruction is decomposed into patches of 8 by 8 pixels, separated by a single pixel.

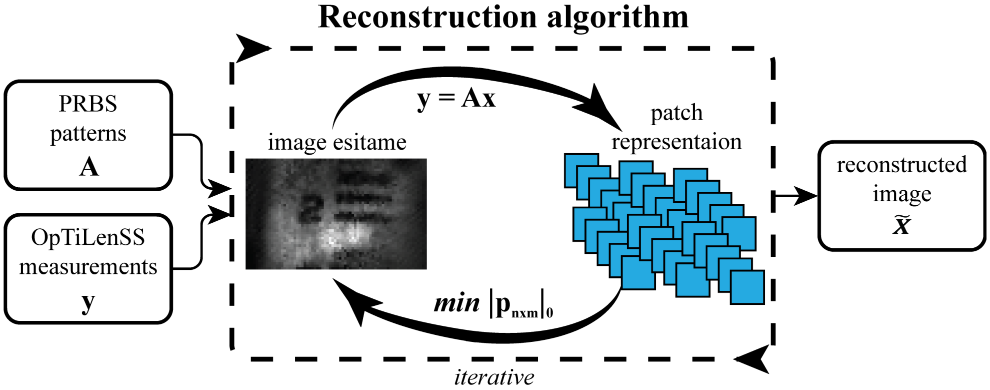

Figure 3.3: The reconstruction algorithm is fed the collected OpTiLenSS compressed measurements y, and the know pseudorandom binary patterns A. The iterative algorithm generates an image estimate then deconstructs the image into 8 by 8 patches. The patches are transform by a DFT basis and sparsified, then inverse transformed and reconstructed back into a sparse image estimate. This process is iterated until the sparsity is maximized while the image estimate maintains fidelity of the measurement vector.

These patches are transformed into a discrete Fourier transform (DFT) basis and thresholded depending on the sparsifying regularization parameter λ. The larger choice for λ will increase the sparsity of the reconstructed image. The patches are then inverse transformed and stichted back together to reform the image estimate. The estimate measurement vector from this sparse image estimate is constrained by the true measurement vector, and is iterated back into the patch form until a final image is reconstructed. Each iteration in the minimization algorithm increases the sparsity while improving the reconstruction image quality.

3.3.2 Resolution target

To demonstrate this approach, we a USAF resolution target at the image plane and reconstruct the images using 500, 1000, and 2000 pulse measurements. In the results shown here, these measurements are averaged ten times to improve the signal-to-noise ratio however with greater optical power this will be unnecessary. Figure 4 shows CS reconstructions using only 15.5%, 31%, and 62% of the samples required by Nyquist corresponding to an imaging frame rate of 18, 9, and 4.5 kHz, due to required averaging. Here we use 10 averages of the returned signal to reduce noise, but reduces the potential frame rate by a decade.

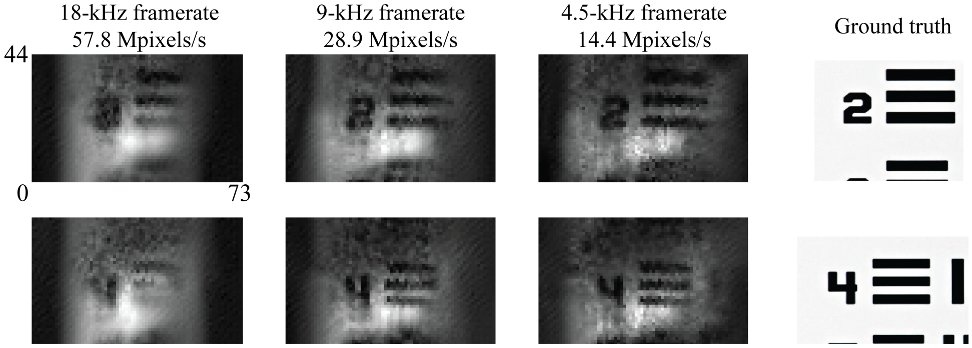

Figure 3.4: The idler is projected to 44x73 pixels (3,212 pixels) over a 1.7-mm by 1.2-mm area and onto a USAF resolution target test object. We show results using 500, 1000, and 200 measurements, or 15.5%, 31%, and 62% of samples required by Nyquist. We see successful reconstruction of the resolution target with 1000 samples, or 31% compression and a 9-kHz frame rate.

3.4 Conclusion

We use nonlinear mixing and propagation in optical fiber to demonstrate an optical time lens spectral shaper to produce a pulse source with unique binary spectral patterns encoded on each pulse. This binary spectral patterning is combined with a two-dimensional spectral projector to complete a single pixel camera. We are able to project over 3000 binary spectral features at a 90-MHz refresh rate, allowing for over a million frames per second single pixel imaging speeds. We demonstrate our proof of concept system with a USAF resolution target, show reconstructions using from 15% to 62% of what is required by Nyquist.

References

Brynk, Tomasz, Anatolii Laptiev, Oleksandr Tolochyn, and Zbigniew Pakiela (2012). “The method of fracture toughness measurement of brittle materials by means of high speed camera and DIC”. In: *Computational Materials Science* 64, pp. 221–224.

Huang, Zhen-Li, Hongyu Zhu, Fan Long, Hongqiang Ma, Lingsong Qin, Yongfeng Liu, Jiuping Ding, Zhihong Zhang, Qingming Luo, and Shaoqun Zeng (2011). “Localization-based super-resolution microscopy with an sCMOS camera”. In: *Optics Express* 19.20, pp. 19156–19168.

H6D-400C MS (2019). H6D-400C. Hasselblad.

the world's most versatile family of high speed camera systems! (2019). MEMRECAM HX-5e. NAC Image Technology.

Tonouchi, Masayoshi (2007). “Cutting-edge terahertz technology”. In: *Nature photonics* 1.2, p. 97.

Onaka, Takashi, Hideo Matsuhara, Takehiko Wada, Naofumi Fujishiro, Hideaki Fujiwara, Miho Ishigaki, Daisuke Ishihara, Yoshifusa Ita, Hirokazu Kataza, Woojung Kim, et al. (2007). “The infrared camera (IRC) for AKARI–design and imaging performance”. In: *Publications of the Astronomical Society of Japan* 59.sp2, S401–S410.

Oh, Wang-Yuhl, BE Bouma, N Iftimia, SH Yun, R Yelin, and GJ Tearney (2006). “Ultrahigh-resolution full-field optical coherence microscopy using InGaAs camera”. In: *Optics express* 14.2, pp. 726–735.

Grulkowski, Ireneusz, Michalina Gora, Maciej Szkulmowski, Iwona Gorczynska, Daniel Szlag, Susana Marcos, Andrzej Kowalczyk, and Maciej Wojtkowski (2009). “Anterior segment imaging with Spectral OCT system using a high-speed CMOS camera”. In: *Optics express* 17.6, pp. 4842–4858.

Slyper, Ronit, Ivan Poupyrev, and Jessica Hodgins (2011). “Sensing through structure: designing soft silicone sensors”. In: *Proceedings of the fifth international conference on Tangible, embedded, and embodied interaction*. ACM, pp. 213–220.

Song, Young Min, Yizhu Xie, Viktor Malyarchuk, Jianliang Xiao, Inhwa Jung, Ki-Joong Choi, Zhuangjian Liu, Hyunsung Park, Chaofeng Lu, Rak-Hwan Kim, et al. (2013). "Digital cameras with designs inspired by the arthropod eye". In: *Nature* 497.7447, p. 95.

Donoho, David L et al. (2006). "Compressed sensing". In: *IEEE Transactions on information theory* 52.4, pp. 1289–1306.

Eldar, Yonina C and Gitta Kutyniok (2012). *Compressed sensing: theory and applications*. Cambridge University Press.

Wallace, Gregory K (1992). "The JPEG still picture compression standard". In: *IEEE transactions on consumer electronics* 38.1, pp. xviii–xxxiv.

Marcellin, Michael W, Michael J Gormish, Ali Bilgin, and Martin P Boliek (2000). "An overview of JPEG-2000". In: *Proceedings DCC 2000. Data Compression Conference*. IEEE, pp. 523–541.

Duarte, Marco F, Mark A Davenport, Dharmpal Takhar, Jason N Laska, Ting Sun, Kevin F Kelly, and Richard G Baraniuk (2008). "Single-pixel imaging via compressive sampling". In: *IEEE signal processing magazine* 25.2, pp. 83–91.

Chan, Wai Lam, Kriti Charan, Dharmpal Takhar, Kevin F Kelly, Richard G Baraniuk, and Daniel M Mittleman (2008). "A single-pixel terahertz imaging system based on compressed sensing". In: *Applied Physics Letters* 93.12, p. 121105.

Welsh, Stephen S, Matthew P Edgar, Richard Bowman, Phillip Jonathan, Baoqing Sun, and Miles J Padgett (2013). "Fast full-color computational imaging with single-pixel detectors". In: *Optics express* 21.20, pp. 23068–23074.

Ma, Jianwei (2009). "Single-pixel remote sensing". In: *IEEE Geoscience and Remote Sensing Letters* 6.2, pp. 199–203.

Sun, Ming-Jie, Matthew P Edgar, David B Phillips, Graham M Gibson, and Miles J Padgett (2016a). "Improving the signal-to-noise ratio of single-pixel imaging using digital microscanning". In: *Optics express* 24.10, pp. 10476–10485.

Sun, Ming-Jie, Matthew P Edgar, Graham M Gibson, Baoqing Sun, Neal Radwell, Robert Lamb, and Miles J Padgett (2016b). "Single-pixel three-dimensional imaging with time-based depth resolution". In: *Nature communications* 7, p. 12010.

Shin, Jaewook, Bryan T Bosworth, and Mark A Foster (2016). "Single-pixel imaging using compressed sensing and wavelength-dependent scattering". In: *Optics letters* 41.5, pp. 886–889.

Shin, Jaewook, Bryan T Bosworth, and Mark A Foster (2017). “Compressive fluorescence imaging using a multi-core fiber and spatially dependent scattering”. In: *Optics letters* 42.1, pp. 109–112.

Bosworth, Bryan T, Jasper R Stroud, Dung N Tran, Trac D Tran, Sang Chin, and Mark A Foster (2015). “High-speed flow microscopy using compressed sensing with ultrafast laser pulses”. In: *Optics express* 23.8, pp. 10521–10532.

Stroud, Jasper R, Bryan T Bosworth, Dung N Tran, Trac D Tran, Sang Chin, and Mark A Foster (2016). “72 MHz A-scan optical coherence tomography using continuous high-rate photonically-enabled compressed sensing (CHiRP-CS)”. In: *CLEO: Science and Innovations*. Optical Society of America, SM2I–1.

Guo, Qiang, Hongwei Chen, Zhiliang Weng, Minghua Chen, Sigang Yang, and Shizhong Xie (2015). “Compressive sensing based high-speed time-stretch optical microscopy for two-dimensional image acquisition”. In: *Optics express* 23.23, pp. 29639–29646.

Stroud, Jasper R and Mark A Foster (2017). “High-speed compressive measurement using a time-lens spectral shaper”. In: *2017 Conference on Lasers and Electro-Optics (CLEO)*. IEEE, pp. 1–1.

Salem, Reza, Mark A Foster, and Alexander L Gaeta (2013). “Application of space–time duality to ultrahigh-speed optical signal processing”. In: *Advances in Optics and Photonics* 5.3, pp. 274–317.

Xiao, Shijun, Andrew M Weiner, and Christopher Lin (2004). “A dispersion law for virtually imaged phased-array spectral dispersers based on paraxial wave theory”. In: *IEEE journal of quantum electronics* 40.4, pp. 420–426.

Chapter 4

All-optical demultiplexing of Nyquist OTDM signal using a biorthogonal Nyquist gate

4.1 Introduction

Due to the need for greater capacity and flexibility, optical communications research has recently focused on the use of orthogonal multiplexing to achieve Tbit/s communication systems while maintaining high spectral efficiency. In orthogonal multiplexing, the orthogonality condition between multiplexed channels eliminates the need for guard bands or intervals and allows for significant channel overlap in the time or frequency domains, thus improving the superchannel's spectral efficiency (Nyquist, 1928; Ellis and Gunning, 2005; Jansen et al., 2009). Furthermore, orthogonal multiplexing coupled with higher-order modulation techniques can increase the net spectral efficiency to the Shannon limit (Essiambre et al., 2010).

Originating from wireless and wideband communication, orthogonal frequency division multiplexing (OFDM) systems combine orthogonal spectral channels with overlap in the frequency domain, removing spectral guard bands. These channels are readily demultiplexed using a fast Fourier transform (FFT) circuit. Optical OFDM systems have been demonstrated reaching 0.89 Bd/hertz and 3.37 bits/s/hertz spectral efficiency at 1 Tbits/s (Ma et al., 2009) using digital signal processing (DSP) to up and down convert the orthogonal channels. However, the limit to these systems becomes the speed of the FFT executed in DSP, where electronics ultimately restrict the data rate. An all-optical method of demultiplexing optical OFDM using an optical FFT circuit was demonstrated to achieve 0.78 Bd/hertz and 6.3 bits/s/hertz spectral efficiency at a superchannel capacity of 26 Tbits/s (Hillerkuss et al., 2011). This method uses an all-optical FFT circuit to demultiplex the optical OFDM superchannel; the all-optical FFT is constructed from optical interferometers, delay lines and phase shifters to cause constructive or deconstructive interference of the orthogonal subchannels followed by narrow temporal gating with an array of electroabsorption modulators to reject intersymbol interference (ISI) (Hillerkuss et al., 2010). This technique dramatically increases the potential superchannel capacity of optical OFDM, but is challenged by the implementation complexity of the all-optical FFT.

The Fourier counterpart to optical OFDM, Nyquist optical time division multiplexing (OTDM), combines orthogonal temporal channels with overlap in the time domain. Relative to optical OFDM, the ideal rectangular spectrum of Nyquist OTDM reduces the effects of dispersion while reaching 1 Bd/hertz spectral efficiency (Sakamoto et al., 2011; Mulvad et al., 2010; Hillerkuss et al., 2012). Furthermore, Nyquist OTDM has a reduced peak to average power ratio (PAPR) relative to optical OFDM, mitigating impairments from fiber nonlinearities (Hirooka and Nakazawa, 2012). Recent demonstrations of Nyquist OTDM systems using high speed electronic circuitry and DSP (Richter et al., 2014; Zhang et al., 2014), have achieved 0.93 Bd/hertz with 1.86 bits/s/hertz spectral efficiency at 250 Gbit/s.

Higher baud rates demand demultiplexing in the analog domain, but the temporal overlap in Nyquist OTDM makes this process difficult to achieve without introducing ISI from neighboring temporal subchannels. Specifically, extracting a Nyquist OTDM subchannel has been demonstrated using a homodyne receiver with a Nyquist local oscillator to convert the signal to baseband and approximately integrate using an electronic low pass filter (LPF) (Miyoshi, Kubota, and Ohashi, 2013; Sakamoto, 2014; Harako et al., 2014), reaching spectral efficiencies of 1 Bd/hertz at up to 4.8 bits/s/hertz on an 80 GBd superchannel. Although the bandwidth of the electronics does not limit the bandwidth of the fully multiplexed Nyquist OTDM data signal, low-pass filtering cannot truly replace the integral in the orthogonality condition of Eq. (3) below, and therefore introduces ISI.

In contrast to electronic approaches, all-optical demultiplexing maintains the information in the optical domain, while isolating a subchannel of interest. This is particularly beneficial if further optical processing or routing is to be employed but can also be used purely for receiving a subchannel of interest. With an increasing demand for flexibility in optical networks, techniques for all-optical multiplexing, demultiplexing and bandwidth conversion have become essential in increasing channel elasticity (Gerstel et al., 2012; Tan et al., 2013). Existing all-optical methods to demultiplex Nyquist OTDM signals use an ultrashort pulse to optically gate the Nyquist OTDM signal at the Nyquist ISI free point (Nakazawa et al., 2012) and achieve 1 Bd/hertz and 1 bits/s/hertz at 160 Gbits/s. Alternatively, a time lens system can transform the OTDM signal to an OFDM-like signal prior to demultiplexing (Hu et al., 2014a; Hu et al., 2014b) achieving a spectral efficiency of 1 Bd/hertz and 1 bits/s/hertz at 320 Gbits/s. However, to extract a subchannel these approaches rely on either a narrow temporal gate or spectral filter to approximate a delta function, creating a tradeoff between the ISI and signal power of the extracted subchannel and thus limiting the realizable degree of higher order modulation. Furthermore, neither of these approaches yield an extracted subchannel with identical properties (e.g. bandwidth and pulse-shape) to the original superchannel.

Here we present an all-optical method for demultiplexing Nyquist OTDM superchannels using a temporally scaled Nyquist gate, which we term a biorthogonal Nyquist gate due to the correspondence with biorthogonal wavelets (Mallat, 2008). The Nyquist pulse shape has been used as an ultrashort gate in order reduce walk-off in the nonlinear fiber compared to a Gaussian shape (Hirooka et al., 2015), but the effect of the pulsewidth was not investigated. We show that the orthogonality relationship between the biorthogonal Nyquist gate and the Nyquist OTDM subchannels allows for full elimination of ISI over a finite spectral region of the mixed product, which can be isolated using a spectral filter of finite width, thus eliminating the aforementioned tradeoff between demultiplexed subchannel power and ISI (Stroud and Foster, 2014). Furthermore, proper choice of the scale parameter yields an extracted subchannel with bandwidth and pulse-shape matched to the Nyquist OTDM superchannel source, thus facilitating further optical signal processing prior to remultiplexing as well as routing. Extending the concept in our previous work (Stroud and Foster, 2014), we more thoroughly examine the implementation of this approach and through simulation compare the performance of a biorthogonal Nyquist gate to a conventional narrow gate in the presence of imperfections including non-ideal gate pulse shape, timing jitter, and dispersion. Furthermore, we experimentally demonstrate the BER performance of this approach for demultiplexing of an 80-GBd Nyquist OTDM signal to 10-GBd using nondegenerate four-wave mixing (FWM) in highly nonlinear optical fiber.

4.2 All-Optical Demultiplexing of Nyquist OTDM

The rectangular spectrum of a Nyquist pulse makes it ideal for transmission on band-limited channels by maximizing the utilization of the available spectrum. In Nyquist OTDM, orthogonal channels composed of Nyquist pulses are multiplexed in time with significant temporal pulse overlap. To achieve channel orthogonality these Nyquist pulses are spaced by the inverse of the channel bandwidth causing the peak of one symbol to coincide with the nulls of the others, illustrated in Fig. 2(a). In a communications system, the primary challenge becomes demultiplexing one of the subchannels without incurring ISI from the others due to this temporal overlap. Notably, while the temporal overlap allows Nyquist OTDM to reach the ideal 1 Bd/hertz symbol spectral efficiency, the overall spectral efficiency (bits/s/hertz) of the communications channel will be determined by the maximum number of bits per symbol that can be differentiated, which will be constrained by the signal to noise ratio and ISI. Thus it is essential to reduce the ISI due to the demultiplexing in order to maximise the system's spectral efficency.

4.2.1 Existing All-Optical Approaches

All-optical demultiplexers are beneficial for applications where it is desirable to maintain the signal in the optical domain and thus avoid optical-to-electrical-to-optical (OEO) conversion such as signal routing and regeneration (Lee et al., 2008; Slavík et al., 2010). Recently demonstrated all-optical approaches to demultiplex Nyquist OTDM signals include using ultrashort optical gating as well as time lens based Fourier transformation(Nakazawa et al., 2012; Hu et al., 2014a). Specifically, narrow time-domain gating of the Nyquist ISI free point has been investigated with promising results (Nakazawa et al., 2012). However, this approach possesses inherent limitations in avoidance of ISI. As illustrated in Fig 2(a), the Nyquist pulse goes to null precisely a time $t = nT_s$, where n is an integer, $T_s = \frac{1}{f_s}$ is the symbol period and f_s is the OTDM baud rate. In order to theoretically eliminated ISI, a gate of infinitely small width would have to be used, presenting an inherit tradeoff. A realistic optical gate of finite temporal width $\triangle t$ will allow ISI through the demultiplexer and, furthermore, reducing $\triangle t$ to decrease ISI will limit the transmitted optical signal power creating a tradeoff between the ISI and signal power. This tradeoff is illustrated by the black curves in Fig. 1, where we plot the demultiplexed subchannel signal's transmission (solid black) and ISI (dashed black) as a function of gate width for a Gaussian gate pulse. Additionally,

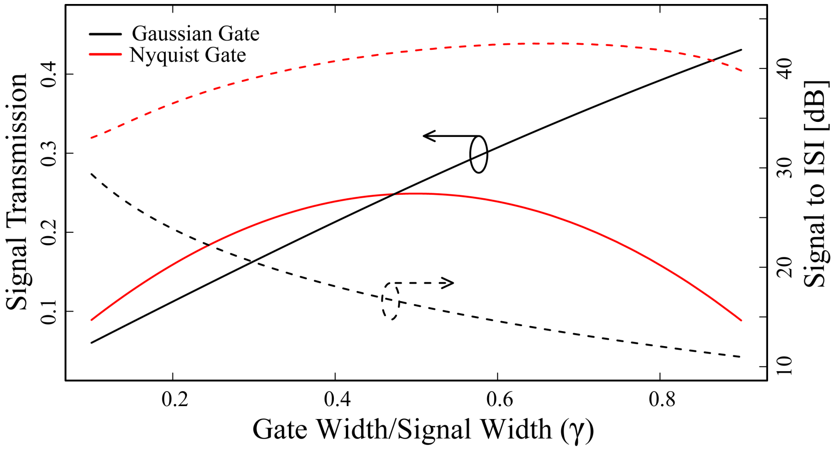

Figure 4.1: With a Gaussian gate, the signal transmission (solid black) is inversely related to the Signal to ISI (dashed black). Using a scaled Nyquist gate and the corresponding scaled spectral bandpass filter, the Signal to ISI (dashed red) is completely due to the Nyquist gate roll-off ($\alpha = 0.15$), while maintaining suitable signal transmission (solid red). There is an ideal operating point with maximum transmission at gate width to signal with ratio or $\gamma = 0.5$, and at this point the demultiplexed subchannel has identical pulse shape to the input.

this tradeoff is not limited to this approach. The alternative time lens based approach, which isolates the subchannel of interest with an optical bandpass filter is effective for reducing the number of nonlinear interactions required in the demultiplexer. However, this approach represents the Fourier equivalent of narrow temporal sampling and yields an equivalent tradeoff between ISI and signal power as a function of the spectral filter bandwidth.

4.2.2 Matched Nyquist Gate

As an alternative to narrow gating, we first investigate matched detection using the orthogonality relationship between the Nyquist OTDM signal and a matched Nyquist gate (Miyoshi, Kubota, and Ohashi, 2013; Sakamoto, 2014; Harako et al., 2014). To begin, we note the orthogonality condition in Eq. (3)

is perfectly satisfied by the DC component of the mixed product between the Nyquist gate pulse

$$\phi_m(t) = sinc\left(t - mT_s\right), \tag{4.1}$$

$$\phi_n(t) = sinc\left(t - nT_s\right), \tag{4.2}$$

$$\int_{-\infty}^{\infty} \phi_m\left(t\right) \phi_n\left(t\right) dt = \delta_{mn}, \tag{4.3}$$

$$h\left(t\right) = \phi_m\left(t\right) \phi_n\left(t\right), \tag{4.4}$$

$$H\left(\omega = 0\right) \equiv \int_{-\infty}^{\infty} h\left(t\right) dt = \delta_{mn}, \tag{4.5}$$

where $h\left(t\right)$ is the mixed product between the Nyquist gate pulse Eq. (1) and matched Nyquist signal pulse Eq. (2), $H\left(\omega\right)$ is the frequency domain equivalent, and δ_{mn} is the Kronecker delta function. In Fig. 2(a) we illustrate a perfectly matched Nyquist gate and the corresponding optical spectrum of the mixed product, $|H(\omega)|^2$, is shown in Fig. 2(b). In Fig. 2(b) we plot both the optical spectrum of the subchannel of interest (signal) and that of the adjacent subchannels (ISI). As is shown, the ISI is completely eliminated at precisely $\omega = 0$, or the DC component, therefore, only the use of an infinitely narrow optical band pass filter to isolate the ISI free point at the center of the spectrum would truly satisfy the orthogonality relationship, as described in Eq. (5). Unfortunately, such a filter would not pass signal power

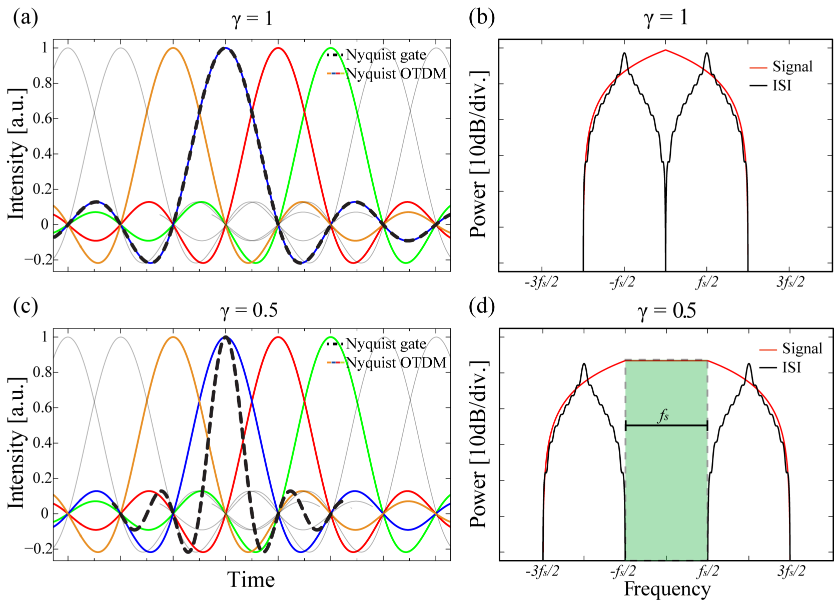

Figure 4.2: (a) Illustration of a perfectly matched Nyquist gate corresponding to $\gamma = 1$. (b) Spectra of the mixed product for the desired channel or $m = n$ (red) and neighboring channels (black), showing zero ISI at $\omega = 0$. In contrast, if we use (c) a scaled Nyquist gate with $\gamma = 0.5$ illustrated in (c), the orthogonality condition between the channels is satisfied over the spectral bandwidth f_s as shown in (d), which can be isolate with physically realizable filters.

and thus a perfectly matched Nyquist gate presents the same tradeoff as the aforementioned approaches using narrow temporal gating.

4.2.3 Biorthogonal Nyquist Gate

To overcome the tradeoff between signal power and ISI common to existing approaches, we investigate demultiplexing with a Nyquist gate of reduced pulse width and a bandpass filter. We scale the Nyquist gate width and filter bandwidth using the parameter γ, representing the ratio of the Nyquist gate width to the Nyquist OTDM symbol width. As shown in Eq. (7), decreasing the Nyquist gate width below $\gamma = 1$, a perfectly matched gate, leads to an orthogonality condition that is satisfied over a range of frequencies in the spectrum of the mixed product,

$$\int_{-\infty}^{\infty} \phi_m \left(\frac{t}{\gamma} \right) \phi_n (t) \, dt = \gamma \delta_{mn}, \tag{4.6}$$

$$H \left(- \left(\frac{1}{\gamma} - 1 \right) \frac{\omega_s}{2} < \omega < \left(\frac{1}{\gamma} - 1 \right) \frac{\omega_s}{2} \right) = \gamma \delta_{mn}. \tag{4.7}$$

Furthermore, as γ and thus the Nyquist gate pulse width decreases, the bandwidth of this ISI-free spectral region increases as given by Eq. (8),

$$\left(\frac{1}{\gamma} - 1 \right) \omega_s \qquad 0 < \gamma \leq 1. \tag{4.8}$$

In Fig. 2(c), we illustrate the time-domain picture of such a biorthogonal gate for the case of $\gamma = 0.5$. The corresponding optical spectrum of the mixed product, $|H(\omega)|^2$, is shown in Fig. 2(d) for both the subchannel of interest (signal) and the adjacent subchannels (ISI). As expected, the $\gamma = 0.5$ biorthogonal Nyquist gate produces no ISI over a finite spectral bandwidth given by Eq. (8) and, after mixing, the subchannel of interest is readily isolated with an optical bandpass filter of matched bandwidth. Thus unlike previous approaches, mixing with a biorthogonal Nyquist gate allows for fully ISI-free demultiplexing of the subchannel of interest using physically realizable gates and filters. The signal to ISI of a Nyquist gate with a roll-off of $\alpha = 0.15$ (dashed red) is shown in Fig 1, this is due completely to the roll-off as illustrated in Fig 3(a), an ideal Nyquist gate fully eliminates ISI. Furthermore, Fig. 1 shows how the Nyquist gate (solid red) compares to a Gaussian gate (solid black) in terms of demultiplexed signal transmission. We find that the signal transmission exhibits an optimum at $\gamma = 0.5$. This optimum results from the interplay between decreasing γ, which decreases the temporal overlap between the Nyquist gate and symbol and thus yields greater loss, and increasing γ, which decreases the ISI free bandwidth thus requiring a narrower filter and therefore greater loss. Mixing with this biorthogonal gate fundamentally yields zero ISI with tolerable signal loss. Additionally, with the choice of $\gamma = 0.5$ and a spectral filter of width f_s, the demultiplexed output possesses the identical bandwidth and pulse shape as the original superchannel and thus can be directly remultiplexed into another f_s baud rate Nyquist OTDM superchannel.

4.3 Analysis with Impairments

The previous section shows that a biorthogonal Nyquist gate can demultiplex a subchannel with zero ISI. However, in a real system impairments will degrade this ideal performance leading to ISI on the demultiplexed subchannel. In this section, we compare how demultiplexing using a biorthogonal Nyquist gate performs under various impairments, including non-ideal gate pulse shape, timing jitter and dispersion. Specifically, we investigate how mixing with a biorthogonal Nyquist gate with $\gamma = 0.5$ and spectral filtering with a bandwidth of f_s performs in comparison to a narrow Gaussian gate operating at the ISI-free point with $\gamma = 0.13$, corresponding to an 870 fs pulse width for a 160 GBd signal to match the experimental optimum found in (Nakazawa et al., 2012). For this comparison we calculate the EVM due to the ISI from all the undesired subchannels. In this paper, we define EVM as the square root of

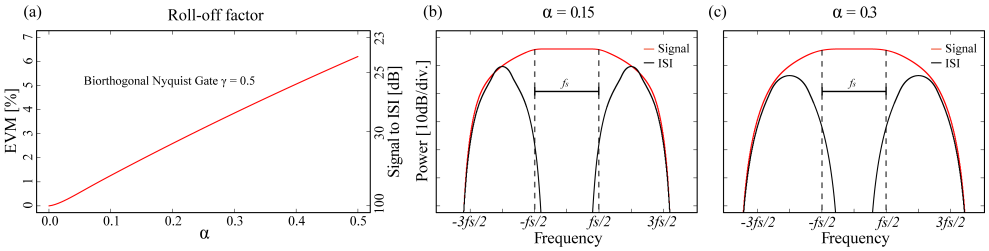

Figure 4.3: (a) The EVM for a raised cosine gate as a function of roll-off factor α. As the roll of factor increases, ISI is introduced into the sides of the ISI free spectral bandwidth as shown in (b) and (c), increasing the EVM.

the inverse signal to interference ratio (Shafik, Rahman, and Islam, 2006).

4.3.1 Raised cosine gate

The ideal rectangular spectra of a Nyquist pulse are not realizable in practice. Thus, we investigate a raised cosine pulse with a roll off factor α to analyze the impact of non-ideal pulse shape,

$$g\left(t\right) = sinc\left(f_s t\right)\frac{cos\left(\pi\alpha f_s t\right)}{1-4\alpha^2 f_s^2 t^2} \qquad 0 \leq \alpha \leq 1. \tag{4.9}$$

The raised cosine pulse becomes an ideal sinc pulse as the roll off factor α approaches zero, but realistically the roll-off factor will be < 0.11 for experimentally realizable optical Nyquist filters (Soto et al., 2013; Preussler, Wenzel, and Schneider, 2014). In Fig. 3, we show the impact of a nonzero roll-off factor on the ISI on the demultiplexed signal. Figure 3(a) shows that the EVM remains below 2% for realistic α values and Figs. 3(b) and 3(c) illustrate the spectral manifestation of the source of ISI at the edges of the filter bandwidth for $\alpha = 0.15$ and $\alpha = 0.3$.

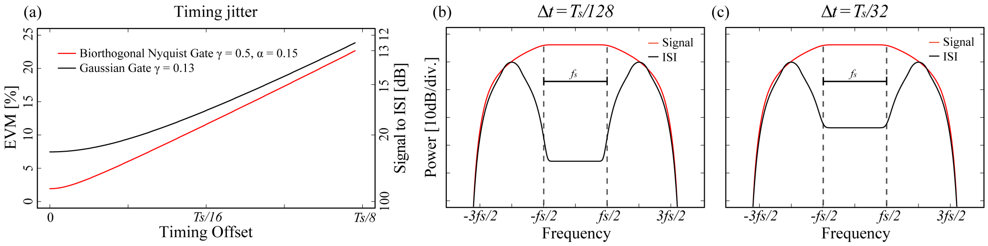

Figure 4.4: (a) The EVM when the Nyquist gate is temporally detuned from peak of the Nyquist OTDM symbol. The timing offset introduces ISI over the entire ISI free bandwidth as shown in (b) and (c).

4.3.2 Timing jitter

All demultiplexing techniques for OTDM signals rely on mixing with a synchronous pulsed gate. Thus the demultiplexers tolerance to timing jitter of this gate is critical because the gate pulse is generally not derived from the same source as the data signal resulting in pulse-to-pulse timing error. This will cause each gate pulse to mix with a different offset from the peak of the OTDM signal. To evaluate the impact of timing jitter, we detune the Gaussian gate and biorthogonal Nyquist gate from the ideal temporal alignment with the Nyquist OTDM symbol and characterize the resulting ISI on the demultiplexed subchannel as shown in Fig. 4. In Fig. 4(a), we plot the EVM of the demultiplexed subchannel as a function of gate timing offset up to one eighth of a symbol period for a biorthogonal Nyquist gate with $\gamma = 0.5$ and $\alpha = 0.15$ as compared to a narrow Gaussian gate with $\gamma = 0.13$ or 870 fs. The biorthogonal Nyquist gate in red shows excellent signal to ISI under small temporal offsets, even with a roll-off factor of $\alpha = 0.15$. However for larger timing offsets the biorthogonal Nyquist gate becomes equivalent to an optical sample, matching the increase in EVM of the narrow Gaussian gate. The

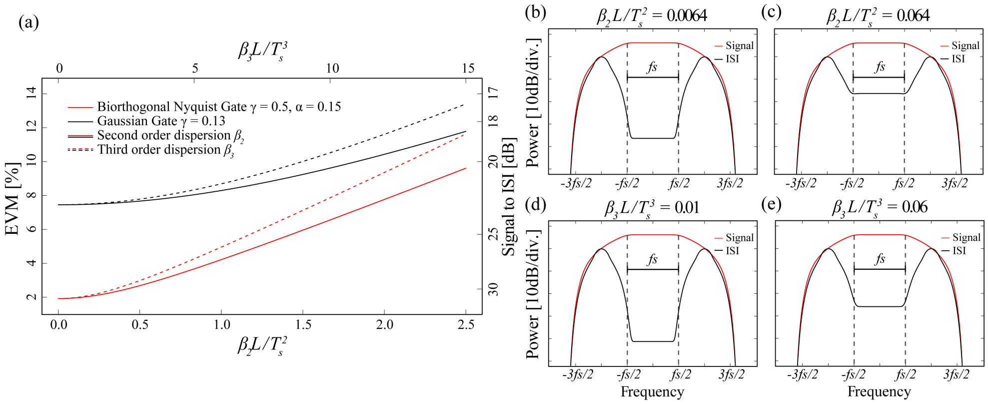

Figure 4.5: (a) The EVM as a function of residual dispersion, showing second order with a solid curve, and third order with a dashed curve. (b)-(e) show the spectral nature of the ISI resulting from residual dispersion for the biorthogonal gate with $\alpha = 0.15$.

spectra of $|H(\omega)|^2$ in Figs. 4(b) and 4(c) show the spectral nature of the ISI resulting from gate timing error.

4.3.3 Dispersion

In long distance ultrahigh-speed OTDM systems, dispersion compensation is critical to correct the pulse distortion before the receiver. However, the dispersive distortions may not be fully removed and puts the burden on the receiver to be resilient to any residual dispersion. Demultiplexing with a biorthogonal Nyquist gate depends on satisfying the orthogonality condition with the Nyquist OTDM signal and dispersion will add a spectral phase term to Eq. (19), degrading the orthogonality condition and introducing ISI.

We show the impact of second- and third-order dispersion on the ISI in Fig. 5(a) with solid and dashed curves, respectively. As is shown, the biorthogonal Nyquist gate performs better than the Gaussian gate for small amounts of dispersion, but in both cases with sufficient residual dispersion the

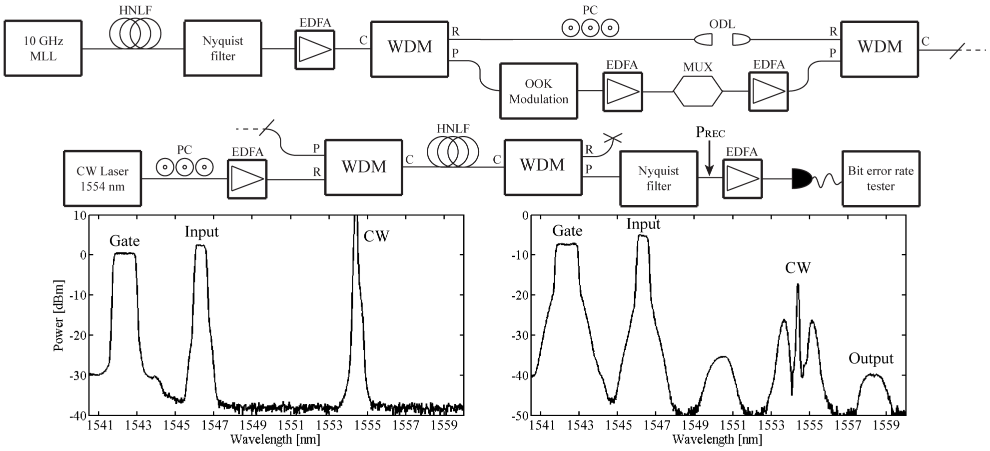

Figure 4.6: A 10-GHz MLL is slightly broadened in HNLF and carved into the signal and pump pulses. The Nyquist signal pulse is modulated and multiplexed then recombined and with the pump. The two Nyquist pulses are propagated through 100m of HNLF with a CW laser and the demultiplexed idler is filtered and detected.

biorthogonal Nyquist gate closely approaches the performance of the narrow Gaussian gate. The spectra of $|H(\omega)|^2$ when the OTDM signal is affected by second- and third-order dispersion are shown in Figs. 5(b)-5(e), illustrating the spectral nature of the ISI.

4.4 Experiment

To experimentally demonstrate this approach we implement the system shown in Fig. 6. We make use of all-optical mixing through nondegenerate four-wave mixing (FWM) between an 80-GBd OOK Nyquist channel at 1546.5 nm, a biorthogonal Nyquist gate at 1542.5 nm, and a continuous wave (CW) laser at 1554.5 nm. This all-optical mixing process generates a new lightwave at an idler wavelength 1558.5 nm. Notably, other all-optical mixing techniques such as sum and difference frequency generation could alternatively be employed, which would eliminate the need for the CW laser. Additionally, pump-degenerate FWM with a root-raised cosine gate pulse can also be implemented instead of a CW laser and Nyquist gate pulse. One advantage of using FWM is that all of the interacting lightwaves lie in the telecommunications band making it ideal for integration with conventional telecommunications hardware and facilitating additional all-optical processing and remultiplexing of the subchannel for further transmission. However, the FWM bandwidth of the HNLF would limit the processing bandwidth of the system, but with standard wavelength division multiplexing (WDM), this would not limit the channel bandwidth or spectral efficiency. In addition, other FWM devices such as silicon waveguides (Ji et al., 2011; Wang et al., 2012) can be implemented with FWM bandwidths well beyond a typical communications channel.

We generate our Nyquist signal and gate pulses by spectrally broadening a 10-GHz passively mode locked laser (MLL) in HNLF followed by filtering with a programmable spectral filter (Finisar Waveshaper 1000s). The 80-GHz Nyquist signal pulses and tunable biorthogonal Nyquist gate are phase and amplitude corrected to achieve Nyquist pulses corresponding to a roll-off factor of $\alpha \simeq 0.1$. The Nyquist signal pulse is separated with a WDM demultiplexer, modulated with an OOK signal at 10 Gbit/s, and temporally multiplexed three times to create an 80 GBd Nyquist signal. The Nyquist signal is amplified and combined with the biorthogonal Nyquist gate and CW laser, which provides the third lightwave for the nondegenerate FWM interaction. Nondegenerate FWM is then implemented in a 100-m HNLF, where a longitudinally varying tension plan with 10-step stair-ramp distribution is applied to reduce stimulated Brillouin scattering (SBS) (Yoshizawa and Imai, 1993). The tension applied to the fiber spectrally shifts the SBS gain

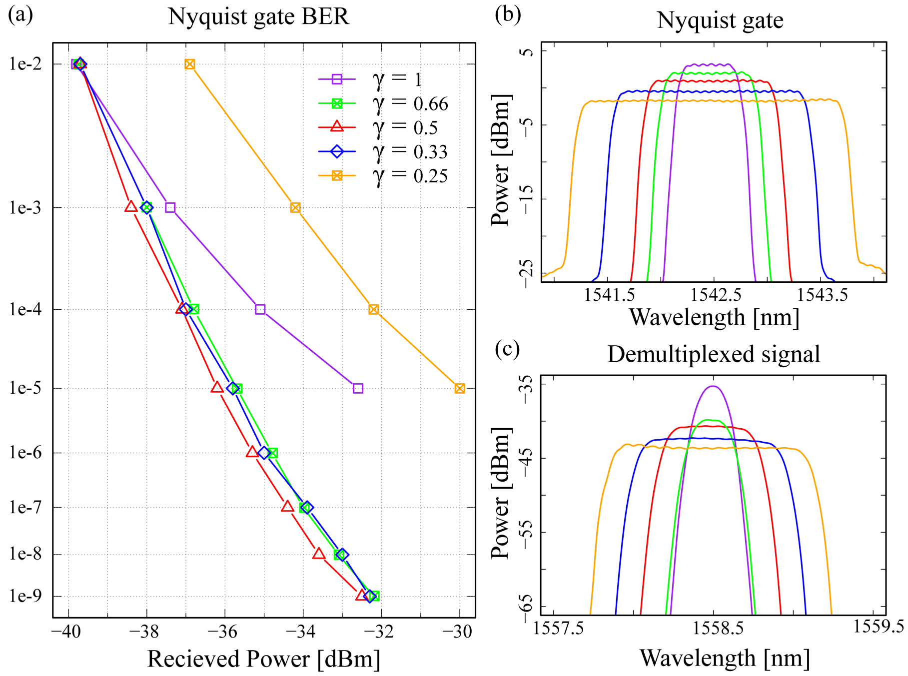

Figure 4.7: (a) The BER curves of an 80 GBd Nyquist OTDM system demultiplexed into eight 10 Gbit/s channels. (b) The spectra of Nyquist gates with 80 GHz, 160 GHz, 240 GHz, and 320 GHz bandwidth. (c) The idler after Nyquist filtering with 30 GHz, 40 GHz, 80 GHz, 120 GHz, and 160 GHz bandwidth.

peak in different sections of the fiber increasing the SBS threshold. The tension also slightly affects the zero-dispersion wavelength, however this dispersive change does not impact the FWM performance given our fiber length and operating wavelengths. The idler is filtered over the ISI free bandwidth with a tunable Nyquist filter then amplified, detected and sent to a bit error rate (BER) tester.

In Fig. 7(a), we compare the BER curves of the demultiplexed signal with a biorthogonal Nyquist gate of different pulse bandwidths illustrated in Fig. 7(b), namely 80 GHz ($\gamma = 1$), 120 GHz ($\gamma = 0.66$), 160 GHz ($\gamma = 0.5$), 240 GHz ($\gamma = 0.33$), and 320 GHz ($\gamma = 0.25$). In Fig. 8(c) we can see the bandwidth change on the detected idler as the Nyquist gate and output filter bandwidths are tuned. The filter bandwidths are 30 GHz, 40 GHz, 80 GHz, 120 GHz, and 160 GHz for the γ values of 1, 0.66, 0.5, 0.33, and 0.25 respectively. When the Nyquist gate is set the theoretically ideal $\gamma = 0.5$ shown in red, with 160-GHz bandwidth and 6.25-ps pulse duration, the ISI free bandwidth and output Nyquist filter are matched to the signal bandwidth of 80 GHz and we can see error free performance across all eight 10 Gbit/s subchannels. When we tune the Nyquist gate to $\gamma = 0.66$ shown in green, the 40-GHz ISI-free region allows for error free transmission with only a slight noise penalty. Similarly, with the Nyquist gate $\gamma = 0.66$ shown in blue, the 120-GHz ISI-free region allows for error free transmission. However, when the Nyquist gate is matched in pulsewidth to the Nyquist signal bandwidth $\gamma = 1$ shown in purple, the output filter of 30 GHz required to achieve sufficient signal power is much larger than the ISI free region, allowing ISI noise to limit the BER performance. Finally, the shortest pulsewidth for the Nyquist gate $\gamma = 0.25$ shown in orange, generates interference from cross-phase modulation inside the ISI-free region, degrading the BER performance.

As expected from our simulations, we find that a Nyquist gate of $\gamma = 0.5$ is the ideal sampling pulse for a Nyquist OTDM signal. The Nyquist gate and output Nyquist filter remove the tradeoff between signal power and signal to ISI noise. This allows us to increase the relative pulse width between the gate to the signal, mitigation nonlinear effects and improving the signal power into the receiver.

4.5 Conclusion

We present a novel method for all-optical demultiplexing of Nyquist OTDM signals. We show a biorthogonal Nyquist gate to demultiplex the signal without interference from neighboring, overlapping subchannels. In the presence of dispersion and timing jitter, the biorthogonal Nyquist gate shows an increased tolerance to ISI, increasing the potential channel spectral efficiencies. In our proof-of-concept experiment, we successfully demultiplex a 10 Gbit/s Nyquist OTDM signal from an 80 GBd carrier by mixing it with a biorthogonal Nyquist gate using nondegenerate FWM. We show error free performance with multiple Nyquist gates, verifying the ideal $\gamma = 0.5$ Nyquist gate. The baud rate scalability and format transparency of this approach paired with high order modulation can facilitate future communication systems with spectral efficiencies close to the Shannon limit.

References

Nyquist, Harry (1928). "Certain topics in telegraph transmission theory". In: *Transactions of the American Institute of Electrical Engineers* 47.2, pp. 617–644.

Ellis, Andrew D and FC Garcia Gunning (2005). "Spectral density enhancement using coherent WDM". In: *IEEE Photonics Technology Letters* 17.2, pp. 504–506.

Jansen, Sander Lars, Itsuro Morita, Tim CW Schenk, and Hideaki Tanaka (2009). "121.9-Gb/s PDM-OFDM transmission with 2-b/s/Hz spectral efficiency over 1000 km of SSMF". In: *Journal of Lightwave Technology* 27.3, pp. 177–188.

Essiambre, René-Jean, Gerhard Kramer, Peter J Winzer, Gerard J Foschini, and Bernhard Goebel (2010). "Capacity limits of optical fiber networks". In: *Journal of Lightwave Technology* 28.4, pp. 662–701.

Ma, Yiran, Qi Yang, Yan Tang, Simin Chen, and William Shieh (2009). "1-Tb/s single-channel coherent optical OFDM transmission over 600-km SSMF fiber with subwavelength bandwidth access". In: *Optics express* 17.11, pp. 9421–9427.

Hillerkuss, D, R Schmogrow, T Schellinger, M Jordan, M Winter, G Huber, T Vallaitis, R Bonk, P Kleinow, F Frey, et al. (2011). "26 Tbit s- 1 line-rate super-channel transmission utilizing all-optical fast Fourier transform processing". In: *Nature photonics* 5.6, p. 364.

Hillerkuss, D, M Winter, M Teschke, A Marculescu, J Li, G Sigurdsson, K Worms, S Ben Ezra, N Narkiss, W Freude, et al. (2010). "Simple all-optical FFT scheme enabling Tbit/s real-time signal processing". In: *Optics express* 18.9, pp. 9324–9340.

Sakamoto, Takahide, Atsushi Kanno, Tetsuya Kawanishi, Nicolas Fontaine, David J Geisler, Ryan P Scott, and SJ Ben Yoo (2011). "160-Gb/s orthogonal time-frequency domain multiplexed QPSK for ultra-high-spectral-efficient transmission". In: *European Conference and Exposition on Optical Communications*. Optical Society of America, We–10.

Mulvad, Hans Christian Hansen, Michael Galili, Leif K Oxenløwe, Hao Hu, Anders T Clausen, Jesper B Jensen, Christophe Peucheret, and Palle Jeppesen (2010). "Demonstration of 5.1 Tbit/s data capacity on a single-wavelength channel". In: *Optics Express* 18.2, pp. 1438–1443.

Hillerkuss, David, Rene Schmogrow, Matthias Meyer, Stefan Wolf, Meinert Jordan, Philipp Kleinow, Nicole Lindenmann, Philipp C Schindler, Argishti Melikyan, Xin Yang, et al. (2012). "Single-laser 32.5 Tbit/s Nyquist WDM transmission". In: *Journal of Optical Communications and Networking* 4.10, pp. 715–723.

Hirooka, Toshihiko and Masataka Nakazawa (2012). "Linear and nonlinear propagation of optical Nyquist pulses in fibers". In: *Optics express* 20.18, pp. 19836–19849.

Richter, Thomas, Markus Nölle, Felix Frey, Colja Schubert, et al. (2014). "Generation and coherent reception of 107-GBd optical Nyquist BPSK, QPSK, and 16QAM". In: *IEEE Photon. Technol. Lett.* 26.9, pp. 877–880.

Zhang, Junwen, Jianjun Yu, Yuan Fang, and Nan Chi (2014). "High speed all optical Nyquist signal generation and full-band coherent detection". In: *Scientific reports* 4, p. 6156.

Miyoshi, Yuji, Hirokazu Kubota, and Masaharu Ohashi (2013). "Nyquist OTDM scheme using optical root-Nyquist pulse and optical correlation receiver". In: *IEICE Electronics Express*, pp. 10–20130943.

Sakamoto, Takahide (2014). "Orthogonal time-frequency domain multiplexing with multilevel signaling". In: *Optics Express* 22.1, pp. 773–781.

Harako, Koudai, David Odeke Otuya, Keisuke Kasai, Toshihiko Hirooka, and Masataka Nakazawa (2014). "High-performance TDM demultiplexing of coherent Nyquist pulses using time-domain orthogonality". In: *Optics Express* 22.24, pp. 29456–29464.

Gerstel, Ori, Masahiko Jinno, Andrew Lord, and SJ Ben Yoo (2012). "Elastic optical networking: A new dawn for the optical layer?" In: *IEEE Communications Magazine* 50.2.

Tan, Hung Nguyen, Takashi Inoue, Takayuki Kurosu, and Shu Namiki (2013). "Transmission and pass-drop operations of mixed baudrate Nyquist OTDM-WDM signals for all-optical elastic network". In: *Optics express* 21.17, pp. 20313–20321.

Nakazawa, Masataka, Toshihiko Hirooka, Peng Ruan, and Pengyu Guan (2012). "Ultrahigh-speed 'orthogonal' TDM transmission with an optical Nyquist pulse train". In: *Optics express* 20.2, pp. 1129–1140.

Hu, Hao, Deming Kong, Evarist Palushani, Michael Galili, Hans Christian Hansen Mulvad, and Leif Katsuo Oxenløwe (2014a). "320 Gb/s Nyquist OTDM received by polarization-insensitive time-domain OFT". In: *Optics Express* 22.1, pp. 110–118.

Hu, Hao, Feihong Ye, Ashenafi Kiros Medhin, Pengyu Guan, Hidehiko Takara, Yutaka Miyamoto, Hans Christian Hansen Mulvad, Michael Galili, Toshio Morioka, and Leif K Oxenlowe (2014b). "Single Source 5-dimensional (space-, wavelength-, time-, polarization-, quadrature-) 43 Tbit/s data transmission of 6 SDM× 6 WDM× 1.2 Tbit/s Nyquist-OTDM-PDM-QPSK". In: *CLEO: QELS_Fundamental Science*. Optical Society of America, JTh5B–10.

Mallat, Stephane (2008). *A wavelet tour of signal processing: the sparse way*. Academic press.

Hirooka, Toshihiko, Daiki Seya, Koudai Harako, Daiki Suzuki, and Masataka Nakazawa (2015). "Ultrafast Nyquist OTDM demultiplexing using optical Nyquist pulse sampling in an all-optical nonlinear switch". In: *Optics express* 23.16, pp. 20858–20866.

Stroud, Jasper R and Mark A Foster (2014). "All-optical demultiplexing of Nyquist OTDM using a Nyquist gate". In: *CLEO: Science and Innovations*. Optical Society of America, SW1J–4.

Lee, Benjamin G, Aleksandr Biberman, Po Dong, Michal Lipson, and Keren Bergman (2008). "All-optical comb switch for multiwavelength message routing in silicon photonic networks". In: *IEEE Photonics Technology Letters* 20.10, pp. 767–769.

Slavík, Radan, Francesca Parmigiani, Joseph Kakande, Carl Lundström, Martin Sjödin, Peter A Andrekson, Ruwan Weerasuriya, Stylianos Sygletos, Andrew D Ellis, Lars Grüner-Nielsen, et al. (2010). "All-optical phase and amplitude regenerator for next-generation telecommunications systems". In: *Nature Photonics* 4.10, p. 690.

Shafik, Rishad Ahmed, Md Shahriar Rahman, and AHM Razibul Islam (2006). "On the extended relationships among EVM, BER and SNR as performance metrics". In: *Electrical and Computer Engineering, 2006. ICECE'06. International Conference on*. IEEE, pp. 408–411.

Soto, Marcelo A, Mehdi Alem, Mohammad Amin Shoaie, Armand Vedadi, Camille-Sophie Brès, Luc Thévenaz, and Thomas Schneider (2013). "Optical sinc-shaped Nyquist pulses of exceptional quality". In: *Nature communications* 4, ncomms3898.

Preussler, Stefan, Norman Wenzel, and Thomas Schneider (2014). “Flat, rectangular frequency comb generation with tunable bandwidth and frequency spacing”. In: *Optics letters* 39.6, pp. 1637–1640.

Ji, Hua, Minhao Pu, Hao Hu, Michael Galili, Leif Katsuo Oxenløwe, Kresten Yvind, Jørn M Hvam, and Palle Jeppesen (2011). “Optical waveform sampling and error-free demultiplexing of 1.28 Tb/s serial data in a nanoengineered silicon waveguide”. In: *Journal of Lightwave Technology* 29.4, pp. 426–431.

Wang, Ke-Yao, Keith G Petrillo, Mark A Foster, and Amy C Foster (2012). “Ultralow-power all-optical processing of high-speed data signals in deposited silicon waveguides”. In: *Optics express* 20.22, pp. 24600–24606.

Yoshizawa, Nobuyuki and Takeshi Imai (1993). “Stimulated Brillouin scattering suppression by means of applying strain distribution to fiber with cabling”. In: *Journal of Lightwave Technology* 11.10, pp. 1518–1522.

Chapter 5

Passive timing stabilization over a 33-km single mode fiber link using temporal imaging

5.1 Introduction

The need for a stable and universal clock has become essential for precise meteorology, navigation, gravitational wave detection and long-distance radio telescopes (Huang, Tjoelker, et al., 2012; Predehl et al., 2012a). State of the art for generating stable clock signals has recently moved from microwave to optical based sources, with the stability of an oscillator is related to its carrier frequency (Gill, 2005). Although precise radio frequency (RF) sources using optical combs have been developed in laboratory (Diddams, 2010; Riehle, 2017), traditional methods for transmitting the time-frequency information is not adequate for long distance distribution an optical clock source. Environmental effects on optical links induce delay fluctuations that distort the phase of the clock signal, reducing the accuracy, and limiting the synchronization between master and slave clocks (Sinclair et al., 2014). The spread of technology and demand for speed require new optical methods for transmitting these precise optical clocks to meet these needs and enable precise communication around the globe and beyond.

Demonstrations of optical time-frequency transfer over fiber links have shown a lot of promise. Stabilized links with fluctuations on the order of femtoseconds can be achieved using actively stabilized links and precise optical frequency comb (Foreman et al., 2007; Predehl et al., 2012b). Methods such as two-way time and frequency transfer (TWTFT) have been extended from fiber to free space, locking optical clocks with excellent accuracy by using the time difference between two optical pulses traveling in opposite directions in the link. This has been shown to stabilize the two clocks with a fractional frequency error below 1×10^{-18} at 1000 seconds averaging time (Giorgetta et al., 2013). However, TWTFT is not compatible with many applications, as it requires expensive and complex optical combs on both the transmitter and receiver and complicated balanced cross-correlators needed to detect the timing signal. Thus this is only a partial solution, challenges arise creating a robust solution for transmitting a stable clock through various environments and applications.

Methods that use a single clock source to distribute time-frequency information are called one-way time and frequency transfer (OWTFT) are more robust and practical for stabilizing a remote link (Sprenger et al., 2009). Generally, a probe signal is sent down the link and returned to determine the environmental error induced in the link. This phase error in the link is assumed to be the same in both directions in the link, so the returned probe is corrupted by twice the phase noise in the link (Levine, 2008; Kumagai et al., 2009). To compensate this error, the transmitted clock signal must be adjusted depending on the detected error on the probe. Modern optical OWTFT in fiber and free space systems use RF mixing to determine the phase error on the returned probe and correct it with active control loop using phase shifters (Wang et al., 2012; Chen et al., 2017). However, these techniques are limited by the speed and accuracy of the compensation devices, such as piezo fiber stretchers and thermal controllers, as well as by the complexity of measuring the link phase noise.

Techniques for passive stabilization using RF mixing for phase conjugation or combining multiple signals to eliminate noise have shown promising results (Li et al., 2014b; Li et al., 2014a). However, these techniques are also limited by the bandwidth and distortion of the analog electronics. An all-optical method has been introduced using nonlinear phase conjugation, but this system requires fine optical filters, limiting the operation to extremely high clock rates of tens of GHz or more (Guo et al., 2016). More flexible and robust OWTFT systems are needed for high-precision time-frequency transfer in extreme environments. We propose a passive all-optical one-way time and frequency transfer system using simple optical components and material properties, allowing us to transmit a stable clock over an optical link with extremely low latency and a flexible clock rate.

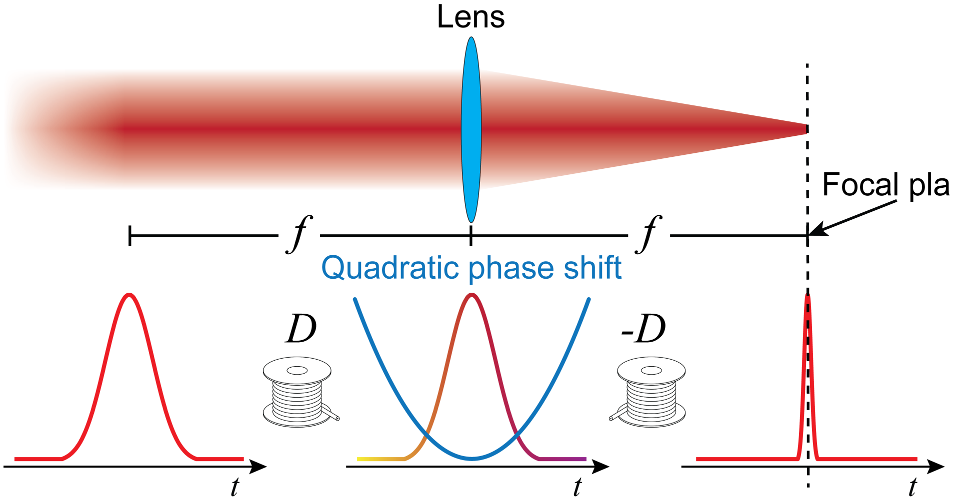

Figure 5.1: a) The energy of the pump photon in FWM will change depending on the arrival time of the probe pulse. b) The error in the probe is caused by fluctuations inside the optical link. c) With the proper mapping of pump dispersion and fiber link dispersion we can send a stable clock to a remote site.

5.2 Stabilization using temporal imaging

The operating principle of our system relies on the temporal imaging based on an optical time lens (Kolner and Nazarathy, 1989). With the analogy diffraction of a beam propagating in space and the dispersion of a optical pulse through fiber, we can draw upon techniques used in spatial optics to implement them in the time domain. The most important of these effects is the lens, able to focus a beam of light on to a single spot. Further, a lens can reduce, magnify or Fourier transform an image, allowing for spatial control of light.

5.2.1 Optical time lens

Figure 1 shows how a spatial lens and time lens are analogous with the lens imparting a quadratic phase shift to create the lens effect. To achieve the necessary quadratic spectral phase shift, we note that the frequency is the derivative of phase, meaning a quadratic phase shift is a linear frequency shift. Using dispersion in optical fiber, we can generate a linear frequency shift that can be applied to a pulse using four-wave mixing (FWM). This type of FWM time lens has been used in a variety of signal processing techniques including temporal magnification and pulse shaping (Salem, Foster, and Gaeta, 2013). This method takes advantage of the large optical bandwidth available in the C-band as well as the large phase shift that can be applied using dispersion (Bennett and Kolner, 2000).

We use this chirped pump FWM to induce an quadratic phase shift that corresponds to the error in the optical link, resulting in a focusing of the converted idler. This nonlinear mixing produces a clock signal that changes in wavelength depending on the error in the link. Phase fluctuations caused by temperature changes that modulate the effective index of the link, resulting in the arrival time of the probe signal shown in blue in Fig. 2 to vary. We can easily achieve the energy or wavelength to time mapping in the pump pulse using dispersion in optical fiber. In order to correct for the link distortions the amount of dispersion in the pump must be chosen to match the dispersion in the link. With a proper dispersion ratio between the link and the pump, the clock signal will provide a stable time frequency signal at the remote site.

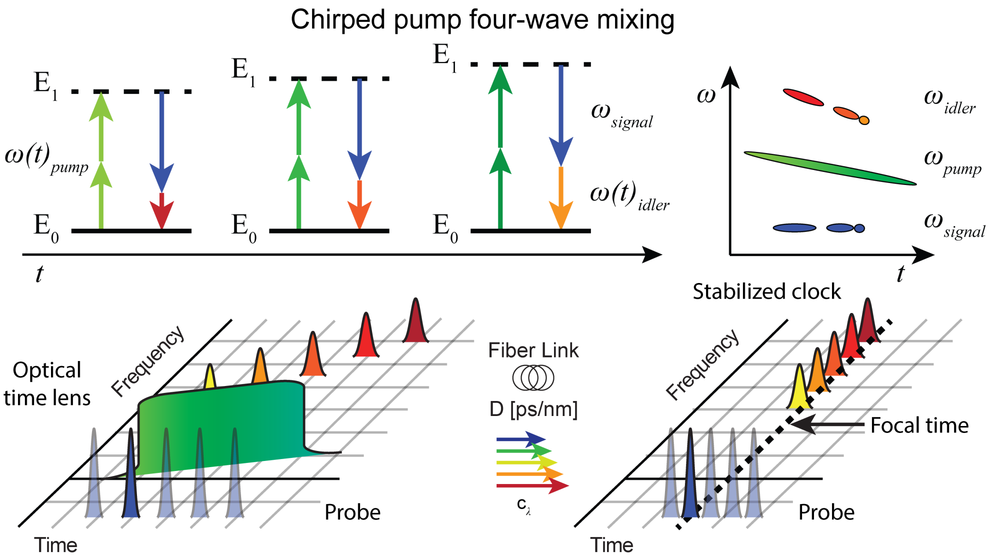

Figure 5.2: a) The energy of the pump photon in FWM will change depending on the arrival time of the probe pulse. b) The error in the probe is caused by fluctuations inside the optical link. c) With the proper mapping of pump dispersion and fiber link dispersion we can send a stable clock to a remote site.

5.2.2 Link error compensation

We show the ideal operating conditions of our proposed system in Fig 2, where the returned probe with twice the link error Δt, is mapped to different wavelengths. With the proper mapping, the clock signal will change wavelengths and will arrive through the link with no effective Δt. To determine this relation, we describe how the probe and clock signal propagate through the link. The propagation time of the probe can be described as,

$$\tau_{probe} = \tau_{center} + D_{link}\Delta nm_{probe} + error_{link}\,(t) \tag{5.1}$$

where τ_{center} is the propagation time for some reference wavelength λ_{center}, used to describe the dispersion D_{link} in the fiber link, and Δnm_{probe} is the difference between our probe and reference wavelengths. The probe wavelength will not change, so the only time dependent variable is the link error denoted $error_{link}$, but we assume that this varies slower than the round trip time through the link. The clock signal is generated from the returned probe pulse,

$$\tau_{signal} = \tau_{center} + 2\tau_{probe} + D_{link}\Delta nm_{signal}\left(t\right) + error_{link}\left(t\right) \tag{5.2}$$

The relationship between the wavelength of the clock signal and the error in the link is based on the degenerate FWM with the dispersed pump as

$$\lambda_{signal} = 2\left(\lambda_{pump} + 2\frac{error_{link}\left(t\right)}{D_{pump}}\right) - \lambda_{probe} \tag{5.3}$$

$$\Delta nm_{signal}\left(t\right) = \left(2\lambda_{pump} - \lambda_{probe} - \lambda_{center}\right) + 4\frac{error_{link}\left(t\right)}{D_{pump}} \tag{5.4}$$

By solving for Eq 2, we can see that the propagation time of the signal depends on the link error, as well as the pump dispersion D_{pump}.

$$\begin{aligned}\tau_{signal} &= 3\tau_{center} + 2D_{link}\Delta nm_{probe} + \\ &D_{link}\left(\left(2\lambda_{pump} - \lambda_{probe} - \lambda_{center}\right) + 4\frac{error_{link}\left(t\right)}{D_{pump}}\right) + 3error_{link}\left(t\right)\end{aligned} \tag{5.5}$$

To stabilize the link, we want to set the temporal derivative to zero.

$$\frac{d\tau_{signa}}{dt} = 0 = 4\frac{D_{link}}{D_{pump}}\frac{derror_{link}\left(t\right)}{dt} + 3\frac{derror_{link}\left(t\right)}{dt} \tag{5.6}$$

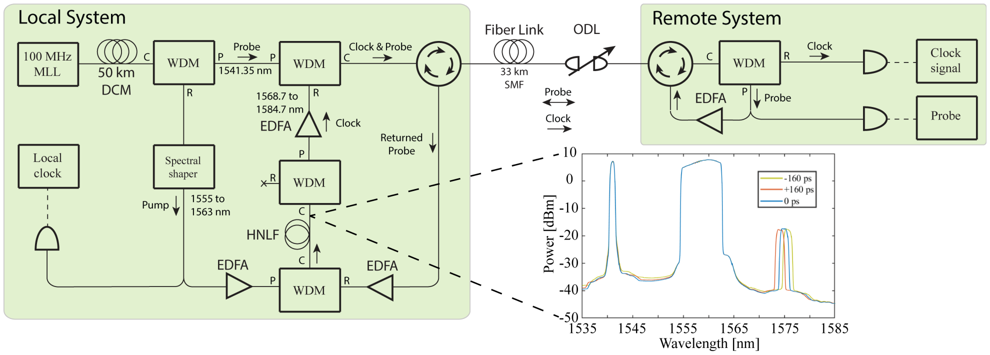

Figure 5.3: The passive stabilization system is shown here using a 100 MHz MLL to both send a probe down the 33 km link and provide a pump to convert the returned probe to different wavelengths depending on the probe timing. Three different ODL positions of -160 ps, 0 ps, and +160 ps are shown inset.

This gives us the simple solution relating the time lens dispersion D_{pump}, to the dispersion in the fiber link D_{link}.

$$D_{pump} = -\frac{4}{3} D_{link} \tag{5.7}$$

We can determine this result analytically remembering that we use degenerate FWM with the probe that has twice the fluctuation in the link. Therefore, the clock signal wavelength is shifted relative to link error shift is four times larger compared to the time to wavelength mapping of the clock dispersion. Because the clock signal sees the link error three times, we find this $-\frac{3}{4}$ ratio in Eq 7 between the pump and signal dispersion.

We can easiily select the approprate dispersion on the pump, allowing for passive cencelation of the timing noise through the fiber link. The actual dispersion value in conjunction with the amount of pump pulse bandwidth used determines the compensation range of the system.

5.3 Experiment

Our system uses a 100 MHz mode-locked laser (MLL) referenced to a 10 MHz rubidium frequency source to generate our stable optical clock signal. The large bandwidth of the MLL is used to produce a probe pulse train at 1541.3 nm and a pump pulse train at 1559 nm. The probe is sent down and back through the link, where it experiences the delay fluctuations from the link twice.

The returned probe is mixed via FWM in a highly nonlinear fiber (HNLF) with the pump pulse that has been dispersed by a dispersion compensation module (DCM) that spreads the 8-nm pump pulse to 6.8 ns. Figure 3 is the system setup, our 33 km link including an optical delay line is between dual circulators to separate the returned probe and clock signal at the transmitter and receiver respectively. The insert in Fig. 3 shows the spectra with the probe at three delays and the corresponding wavelength shift in the idler around 1576 nm. The idler is then sent through the 33 km single mode fiber (SMF) link, where the total propagation time depends on both the link fluctuations as well as the idler wavelength through the link dispersion. The error to wavelength mapping in our system is 0.16 nanoseconds per nanometer, resulting in up to 14 nm shifts in the idler. By adjusting the focal length of the time lens, the link dispersion of 33 km in this experiment, the error to wavelength mapping would change accordingly.

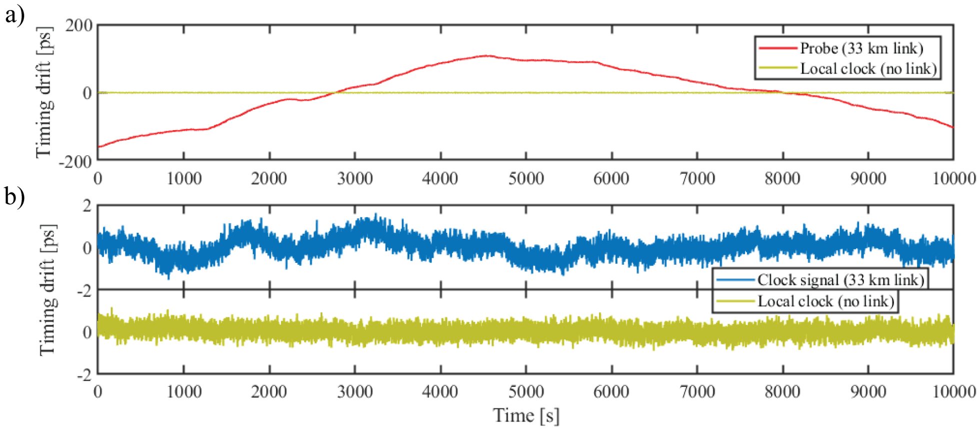

Figure 5.4: a) The timing drift of the probe is shown in red, drifting over 300 picoseconds in less than three hours. b) The local clock shown in yellow is compared to the signal clock in blue, both only drifting less than two picoseconds.

5.4 Results

We test our system using a time interval counter to determine the difference between a test signal and the local clock. Long term tests of the 33 km free running link are shown compared to the local clock signal in Fig. 4. The probe signal in the 33 km link shown in red has a standard deviation of 73 ps while the local clock only has a standard deviation of 0.23 ps over a few hours or 1×10^4 seconds. The passively stabilized clock signal in blue has only minor fluctuations, a standard deviation of 0.4 ps over 1×10^4 seconds.

The Allan deviation is calculated for the three different signals in Fig. 5, the local clock signal in yellow, the probe through the 33 km link in red, and the clock signal through the 33 km link in blue. We see over two decades of improvement in the clock signal at over 1000 seconds averaging time. The Allan deviation calculated for over two days is shown in Fig. 5, where the signal clock continues to fall to 2×10^{-17} deviation.

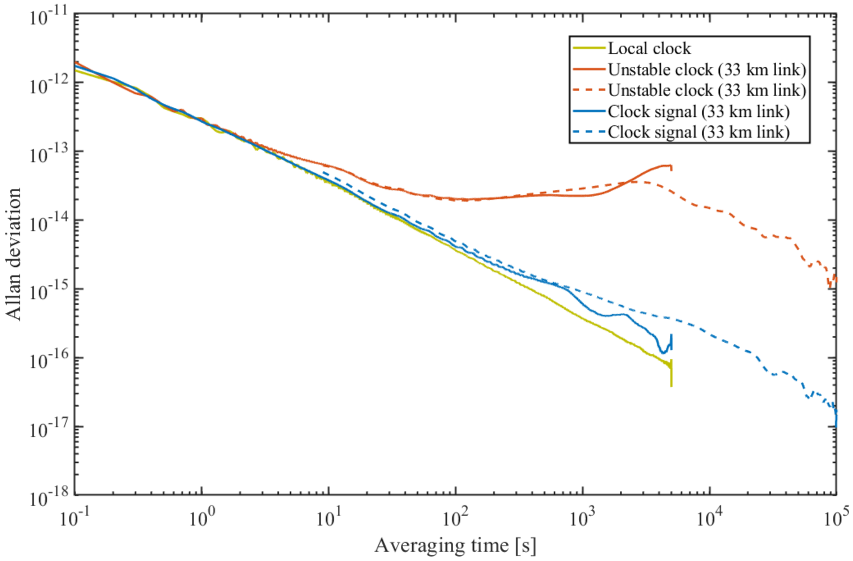

Figure 5.5: a) The Allan deviation of the probe in red, and the signal in blue through a 33 km link over three hours. The stabilized clock signal shows over two decades lower Allan deviation compared to the probe, nearly reaching the noise floor of the system shown in yellow. The clock signal deviation continues decrease for data taken for over two days, shown with a dashed line.

The local clock shown in yellow is the MLL being compared to itself in Fig. 4, where it is limited by the photo-detection process used for the time interval counter. We expect the optical comb source to achiever lower fluctuations using more advanced phase detection schemes. The limits on the clock signal are mainly due to realistic deviations from the ideal ratio in Eq 7 due to dispersion measurement tolerances and higher order dispersion. The proof of concept system shown here is not actively compensated for higher orders of dispersion, limiting our results to about two decades, matching the results we see experimentally in Fig. 5, where the probe and signal are separated by two decades above 1000 seconds averaging time.

The large amount of optical fiber in the DCM limits the performance of our optical frequency comb to 2×10^{-13} at one second. The laser output of the DCM is used as the reference for all the measurements and is defined as our local clock. We use a simple DCM disperser and SMF fiber link pair to take advantage of the dispersion naturally inside a link and because they are readily available; however, dispersion can be provided using other methods. Written dispersion profiles of chirped fiber Bragg gratings and tunable dispersion compensation using spectral shapers make it straightforward to implement this system on a variety of optical links, both fiber and free space, and increase the noise floor of the system (Hill et al., 1994).

5.5 Conclusion

In this paper we present a passive system for transmitting a stable clock signal to a remote location. We use natural dispersion of the fiber link to control the wavelength of the clock to completely compensate for and fluctuations in the link. With a simple relationship between pump and link dispersion, this system is extremely scalable, and the all optical signal possessing is done in less than 100 meters of fiber, minimizing the system latency. The passive control, low latency, and receiver simplicity make the system excellent for turbulent environments, including free space links.

References

Huang, S, RL Tjoelker, et al. (2012). "Stabilized photonic links for deep space tracking, navigation, and radio science applications". In:

Predehl, Katharina, G Grosche, SMF Raupach, Stefan Droste, O Terra, Janis Alnis, Th Legero, TW Hänsch, Th Udem, Ronald Holzwarth, et al. (2012a). "A 920-kilometer optical fiber link for frequency metrology at the 19th decimal place". In: *Science* 336.6080, pp. 441–444.

Gill, Patrick (2005). "Optical frequency standards". In: *Metrologia* 42.3, S125.

Diddams, Scott A (2010). "The evolving optical frequency comb". In: *JOSA B* 27.11, B51–B62.

Riehle, Fritz (2017). "Optical clock networks". In: *Nature Photonics* 11.1, p. 25.

Sinclair, Laura C, Fabrizio R Giorgetta, William C Swann, Esther Baumann, I Coddington, and Nathan R Newbury (2014). "Optical phase noise from atmospheric fluctuations and its impact on optical time-frequency transfer". In: *Physical Review A* 89.2, p. 023805.

Foreman, Seth M, Andrew D Ludlow, Marcio HG De Miranda, Jason E Stalnaker, Scott A Diddams, and Jun Ye (2007). "Coherent optical phase transfer over a 32-km fiber with 1 s instability at 10- 17". In: *Physical Review Letters* 99.15, p. 153601.

Predehl, Katharina, G Grosche, SMF Raupach, Stefan Droste, O Terra, Janis Alnis, Th Legero, TW Hänsch, Th Udem, Ronald Holzwarth, et al. (2012b). "A 920-kilometer optical fiber link for frequency metrology at the 19th decimal place". In: *Science* 336.6080, pp. 441–444.

Giorgetta, Fabrizio R, William C Swann, Laura C Sinclair, Esther Baumann, Ian Coddington, and Nathan R Newbury (2013). "Optical two-way time and frequency transfer over free space". In: *Nature Photonics* 7.6, p. 434.

Sprenger, B, J Zhang, ZH Lu, and LJ Wang (2009). "Atmospheric transfer of optical and radio frequency clock signals". In: *Optics letters* 34.7, pp. 965–967.

Levine, Judah (2008). “A review of time and frequency transfer methods”. In: *Metrologia* 45.6, S162.

Kumagai, Motohiro, Miho Fujieda, Shigeo Nagano, and Mizuhiko Hosokawa (2009). “Stable radio frequency transfer in 114 km urban optical fiber link”. In: *Optics letters* 34.19, pp. 2949–2951.

Wang, B, C Gao, WL Chen, J Miao, X Zhu, Y Bai, JW Zhang, YY Feng, TC Li, and LJ Wang (2012). “Precise and continuous time and frequency synchronisation at the 5× 10-19 accuracy level”. In: *Scientific reports* 2, p. 556.

Chen, Shijun, Fuyu Sun, Qingsong Bai, Dawei Chen, Qiang Chen, and Dong Hou (2017). “Sub-picosecond timing fluctuation suppression in laser-based atmospheric transfer of microwave signal using electronic phase compensation”. In: *Optics Communications* 401, pp. 18–22.

Li, Wei, Wen Ting Wang, Wen Hui Sun, Wei Yu Wang, and Ning Hua Zhu (2014b). “Stable radio-frequency phase distribution over optical fiber by phase-drift auto-cancellation”. In: *Optics letters* 39.15, pp. 4294–4296.

Li, Dawei, Dong Hou, Ermeng Hu, and Jianye Zhao (2014a). “Phase conjugation frequency dissemination based on harmonics of optical comb at 10- 17 instability level”. In: *Optics letters* 39.17, pp. 5058–5061.

Guo, Xiaojie, Xiaocheng Wang, Zhaohui Li, and Yi Dong (2016). “Optical parametric mixer-based passive phase correction for stable transfer of millimeter waves”. In: *Optics letters* 41.19, pp. 4574–4577.

Kolner, Brian H and Moshe Nazarathy (1989). “Temporal imaging with a time lens”. In: *Optics letters* 14.12, pp. 630–632.

Salem, Reza, Mark A Foster, and Alexander L Gaeta (2013). “Application of space–time duality to ultrahigh-speed optical signal processing”. In: *Advances in Optics and Photonics* 5.3, pp. 274–317.

Bennett, Corey V and Brian H Kolner (2000). “Principles of Parametric Temporal Imaging-Part I: System Configuration”. In: *IEEE Journal of Quantum Electronics* 36.4, pp. 430–437.

Hill, KO, F Bilodeau, B Malo, T Kitagawa, S Theriault, DC Johnson, Jacques Albert, and K Takiguchi (1994). “Chirped in-fiber Bragg gratings for compensation of optical-fiber dispersion”. In: *Optics letters* 19.17, pp. 1314–1316.

Chapter 6

Conclusion and future work

6.1 Conclusion

In this thesis I have presented a number of optical systems designed to increase the information flow of an optical network. The information from a image acquired with real time compression can be sent down a spectrally efficient optical link regardless of environmental fluctuations. By sending compressed data, networks are free to service more users and deliver information to the users who need them most. Next generation networks will utilize every technology to increase bandwidth, reliability, and information content on the wire.

My research utilizes ultrafast optics, electro-optics, and dispersion to use light to control light for applications where high-speed signal processing is essential. One of the main advantages of optical-to-optical processing is the compatibly with integrated photonics. Next generation data centers and everyday electronics will include integrated optical components used for extremely high-speed and versatile processing.

6.2 Reaching the limit of information

Nyquist sampling theory has been the backbone of signal acquisition for decades. With the quantity of data acquired daily, more information needs to be extracted and faster. Compressed sensing theory has revolutionized how information is acquired, requiring far fewer samples than Nyquist theory.

The limits of Nyquist sampling are well know, sampling a signal with twice the max signal bandwidth guarantees the acquisition of any signal. However the information bandwidth of most signals is far less than its maximum bandwidth, leading to redundant information being acquired, exhausting communications and signal acquisition systems.

This thesis demonstrates two methods for generating compressed measurements by structuring the illumination on an image. The practical speed of any CS system is determined both by how complicated the optical structure can be and how fast the CS samples are collected. Simply, a CS system is sampled at the rate of the CS measurements, with each measurement containing the information about the structure, which is N-bits complex. For binary modulation, the number of these CS-bits is directly related to the reconstructed resolution of the image. For the line scanning system deployed for our CHiRP-CS OCT, we show CS measurements at 1.44 GHz, and 384 CS-bits per pulse, resulting in 0.55 CS-Tbit/s. Comparatively, the OpTiLenSS system acquires CS measurements at 90 MHz with 3,212 CS-bits per pulse, for a total of 0.29 CS-Tbit/s.

The number of CS-bits per second determines the speed and resolution of a CS system, but the spectral efficiency determines the scalability. The

CS-bit spectral limit is due to the time-bandwidth product of the optical pulse, the more information on a limited spectrum, the longer it will be in time. Including the spectral bandwidth, the CHiRP-CS OCT system achieves 0.115 CS-bit/s/hz and the OpTiLenSS system achieves 0.116 CS-bit/s/hz. This is reaching towards the limit of 1 CS-bit/s/hz that ca be achieved with ideal pulse shaping and coherent sampling.

In order to completely utilize the spectrum to collect information, systems need to maximize the CS-bit/s/hz and adjust the CS measurement rate depending on the application. The CHiRP-CS system is limited in CS-bits per measurements, but can be easily multiplexed to achieve a high spectral efficiency. On the other had, the OpTiLenSS system is much more flexible in trading off between the measurement rate and CS-bit content.

Future systems will need to juggle the measurement rate, bit content, and structure to find the best solution to any problem. With the rise of application based technology it is clear that the best way to extract information is knowing where to look. Compressed sensing systems take full advantage of a priori knowledge while maximizing the output information flow.

6.3 Next generation communications networks

The constant demand for bandwidth has pushed modern networks to the limit. New technology is needed that is more flexible, lower power, smaller, and cheaper. Integrated photonics has started to address this problem at the data center level, moving toward more optical interconnects and signal processing. The total integration of communications electronics and optics on a single chip is in the near future.

In this thesis I have demonstrated two techniques for increasing communication efficiency and reach that are compatible with integrated photonic devices. The optical signal processing can be done at lower powers and smaller area, making it flexible an compatible with CMOS technology.

6.3.1 Spectral efficiency

Although fibers are getting more transparent as more optical wavelengths are viable, every communication system is bandwidth limited. To maximize transmission, communications networks need to be flexible and efficient. Data networks need to improve in spectral efficiency to meet future demands.

In this thesis I present a Nyquist OTDM system that can reach the limits of spectral efficiency. I show ideal demultiplexing conditions with zero intersymbol interference due to the Nyquist pulse shape properties. To further this work, the nonlinear optical signal processing needs to be adopted and realized on a photonic chip.

6.3.2 Remote fiber interconnects

Connecting the world with fiber optics has been inevitable since the first telephone call. While modern technology has been sufficient for connecting large hubs, remote destinations lack coverage. Large transmission distances include large fluctuations in operating conditions, meaning the farther the link, the worse the information rate. Novel techniques for stabilizing optical links are needed to reach every corner of the globe and beyond.

Here I present a passive all-optical method of stabilizing an optical link. Wth only a single clock source, the remote location can receive and send high fidelity data through extreme environments. I show this system on a fiber link, further work would involve demonstrating free space optical link stabilization. The final frontier will soon be illuminated with our communications, new robust and efficient information networks are essential to continued growth.

Jasper R. Stroud

July 2019

3105 North Calvert Street, Baltimore, MD 21218
(510)-325-0516 *jasperstroud@gmail.com*

Summary:

Optical engineer with expertise in nonlinear optical systems using fiber, free space, and integrated platforms. I am an experimentalist with experience with a variety of optical systems for high speed data acquisition, computational imaging, and optical communications networks. Proficient in MATLAB, R, and Python as well as computational techniques including nonlinear wave propagation, statistical modeling, and compressive sensing.

Education:

Johns Hopkins University	*B.S.*	2013
Johns Hopkins University	*Ph.D.*	2019

Research experience and skills:

Johns Hopkins Ultrafast and Nonlinear Photonics Group: (2011 - Present)

<u>Optical communication:</u>

- High precision time transfer over optical links using optical time reversal.
- Spectrally efficient demultiplexing with zero intersymbol interference using Nyquist pulse shaping and nonlinear signal processing.
- Communication networks using amplitude and phase electro-optic modulation with continuous wave and pulsed lasers including high order modulation and multiplexing.

<u>Nonlinear optics:</u>

- Comb generation using CW lasers with highly nonlinear optical fiber or silicon waveguides for multicasting communications signals and pulse generation.
- Time to wavelength conversion using four-wave mixing in an optical time lens.
- Four-wave mixing Bragg scattering for low noise single photon generation.

<u>Integrated photonics:</u>

- Characterization of photonic integrated chips with novel materials and interlayer couplers.
- Finite-difference time-domain electromagnetic modeling of waveguides to optimize nonlinearity, dispersion, and coupling loss.
- Infrared optical parametric oscillator in an amorphous silicon waveguide.
- Pattern detection using nonlinear wave mixing in amorphous silicon waveguides.

<u>High speed imaging:</u>

- Temporal focusing two-photon microscopy using compressed sensing.
- Structured illumination and dispersive mapping for applications in ultrafast microscopy.
- Optical coherence tomography using compressed sensing to increase imaging speed.

<u>Radio frequency sensing:</u>

- Sparse GHz signal detection using compressed sensing with ultrafast laser pulses.
- Photonically assisted analog to digital converter using a photonic sample and hold architecture.

<u>Physically unclonable functions:</u>

- Challenge and response pair authentication using an integrated photonic chaotic resonator for hardware security.

- Information content extraction and analysis.
- Mitigation of machine learning attacks using nonlinearity of amorphous and crystalline silicone waveguides.

Professional activities:

Teaching

Women in science and engineering: (Spring 2019)

Johns Hopkins program for mentoring local high school students to introduce them to STEM research ideas and techniques.

Fiber optic communications: (Fall 2017)

Johns Hopkins lower level undergraduate course focused on introducing research topics.

Optics every day: (Jan. 2017 & 2018)

Johns Hopkins short course on basic optics concepts that are a part of technology we interact with every day. Lab course with multiple hands on optics experiments.

SABES: (2014-2015, 2016-2017)

Baltimore City elementary school mentoring in a local afterschool program to promote STEM education and problem-based thinking.

Professional development

Treasurer of the Optical Society at Johns Hopkins: (2013-2018)

The local student chapter put on social, professional development, and educational outreach events for graduate students working in optics.

Organizer of the Optics and Photonics Conference at Johns Hopkins: (Dec. 2017)

Treasurer and lead organizer for the first Optics and Photonics Conference at Johns Hopkins, designed to unite and foster collaboration in the optics community. We had five invited talks, six student talks and a poster session with over 40 submissions from departments all over campus, as well as surrounding universities.

Peer review: (2016 - Present)

Reviewing journal articles in Optics Express and Optics Letters.

Johns Hopkins Homewood Researcher Safety Committee: (2014 - 2018)

Treasurer then President of the graduate student run laboratory safety committee. Our goal is to keep researchers well informed of safety protocols and provide input for future standards and procedures.

Peer-reviewed work:

Google scholar

https://scholar.google.com/citations?user=i4swAZoAAAAJ&hl=en

Publications in progress

1. Iskandar A. Atakhodjaev, Bryan T. Bosworth, Michael R. Kossey, Brian C. Grubel, Daniel S. Vresilovic, Jasper R. Stroud, Neil MacFarlane, Jesús Villalba, Najim Dehak, A. Brinton Cooper, Mark A. Foster, Amy C. Foster, "Machine Learning Attacks on Nonlinear Silicon Photonic Physical Unclonable Functions", in preparation for Applied Optics Letters.

2. Jasper R. Stroud, L. Li, D. N. Tran, T. D. Tran, S. Chin, and M. A. Foster, "Optical coherence tomography using physical domain data compression to achieve MHz A-scan rates", in preparation for Optics Express.

3. Jasper R. Stroud, O. Okusaga, G. Weaver. N. Mosavi, and M. A. Foster, “Passive timing stabilization over a 33-km single mode fiber link using temporal imaging”, in preparation.

4. Jasper R Stroud and Mark A. Foster. "Optical time-lens spectral shaper for high-speed single-pixel imaging", in preparation.

Journal publications

5. M. Alemohammad, J. Shin, D. N. Tran, Jasper R. Stroud, S. P. Chin, T. D. Tran, and M. A. Foster. "Widefield Compressive Multiphoton Microscopy", Optics letters 43(12), 2989-2992 (2018).

6. Jasper R. Stroud and M. A. Foster, "All-optical demultiplexing of Nyquist OTDM signal using a biorthogonal Nyquist gate," Optics Express 25(26), 33250-33260 (2017).

7. M. Alemohammad, Jasper R Stroud, B. T. Bosworth, and M. A. Foster, “High-speed all-optical Haar wavelet transform for real-time image compression,” Optics Express, 25(9), 9802-9811 (2017).

8. H. F Ting, K. Y. Wang, Jasper R. Stroud, K. G. Petrillo, H. Sun, A. C Foster, and M. A. Foster, “Wavelength multicasting through four-wave mixing with an optical comb source,” Optics Express, 25(8), 9276-9284 (2017).

9. B. T. Bosworth, Jasper R. Stroud, D. N. Tran, T. Tran, S. Chin, and M. A. Foster, "High-speed flow microscopy using compressed sensing with ultrafast laser pulses", Optics Express 23(8), 10521-10532 (2015).

10. B. T. Bosworth, Jasper R. Stroud, D. N. Tran, T. Tran, S. Chin, and M. A. Foster, “Ultrawideband compressed sensing of arbitrary RF frequencies using spectrally-encoded ultrafast laser pulses”, Optics Letters 40(13), 3045-3048 (2015).

Conferences

11. Jasper R. Stroud Neil MacFarlane, A. Brinton Cooper, Mark A. Foster, and Amy C. Foster, “Integrated photonic physical unclonable function using highly nonlinear amorphous silicon”, IEEE International Conference on Group IV Photonics, 2019.

12. Jasper R. Stroud and Mark A. Foster. "Ultrahigh-speed spatial pattern projection using a nonlinear optical time lens for fast single-pixel imaging." CLEO: Applications and Technology. Optical Society of America, 2019.

13. Jasper R. Stroud, Olukayode Okusaga, Gregory Weaver, Nelli Mosavi, and Mark A. Foster. "Passive timing stabilization over a 33-km single mode fiber link using temporal imaging." In 2018 6th IEEE International Conference on Wireless for Space and Extreme Environments (WiSEE), pp. 137-140. IEEE, 2018.

14. Jasper R. Stroud, Olukayode Okusaga, Gregory Weaver, Nelli Mosavi, and Mark A. Foster. "Passive Timing Stabilization over a 33-km Single Mode Fiber Link using Temporal Imaging." In 2018 IEEE Photonics Conference (IPC), pp. 1-2. IEEE, 2018.

15. Jasper R. Stroud and M. A. Foster, "High-speed compressive measurement using a time-lens spectral shaper" Conference on Lasers and Electro-Optics 2017.

16. Jasper R. Stroud, B. T. Bosworth, D. N. Tran, T. D. Tran, S. Chin, and M. A. Foster, "72 MHz A-scan optical coherence tomography using continuous high-rate photonically-enabled compressed sensing (CHiRP-CS)." Conference on Lasers and Electro-Optics 2016.

17. Jasper R. Stroud, B. T. Bosworth, D. N. Tran, T. McKenna, T. Clark, T. D. Tran, S. Chin, M. A. Foster, “Continuous 119.2-GSample/s Photonic Compressed Sensing of Sparse Microwave Signals”, Conference on Lasers and Electro-Optics 2015.

18. B. T. Bosworth, Jasper R. Stroud, D. N. Tran, T. D. Tran, S. Chin, M. A. Foster, “Compressive 39.6-gigapixel/s continuous imaging using spectrally-structured ultrafast laser pulses”, Conference on Lasers and Electro-Optics 2015.

19. B. T. Bosworth, Jasper R. Stroud, D. N. Tran, T. D. Tran, S. Chin, M. A. Foster, “Ultrawideband RF Compressed Sensing Using Spectrally-Encoded Ultrafast Laser Pulses”, Compressed Sensing Theory and its Applications to Radar, Sonar and Remote Sensing 2015.

20. B. T. Bosworth, Jasper R. Stroud, D. N. Tran, T. D. Tran, S. Chin, M. A. Foster, “Compressive ultrahigh-speed continuous imaging using spectrally-structured ultrafast laser pulses”, SPIE 9355, Frontiers in Ultrafast Optics 2015.

21. Jasper R. Stroud, and M. A. Foster, “All-optical demultiplexing of Nyquist OTDM using a Nyquist gate”, Conference on Lasers and Electro-Optics 2014.

22. H. Ting, K. Wang, Jasper R. Stroud, M. A. Foster, and A. C. Foster, "Efficient Wavelength Multicasting through Four-Wave Mixing with a Comb Source," Conference on Lasers and Electro-Optics 2014.

23. K. G. Petrillo, Jasper R. Stroud, and M. A. Foster, “An all-optical sample-and-hold architecture incorporating amplitude jitter suppression”, Conference on Lasers and Electro-Optics 2012.

Patents

B. T. Bosworth, M. A. Foster, Jasper R. Stroud, T. Tran, S. Chin, and D. Tran. "Compressive imaging systems and methods." U.S. Patent 9,645,377, issued May 9, 2017.

Pending patents

J. Shin, Jasper R. Stroud, M. A. Foster, “A minimally-invasive lens-free computational microendoscope”, in preparation.

N. Mosavi, Jasper R. Stroud, M. A. Foster, O. Okusaga, and G. Weaver, “Optical time transfer using optical time reversal”, a disclosed invention.